Seasonal variability of ozone mixing ratios and budgets in the tropical southern Pacific: A GCTM perspective

C.-F. Wei,[1] V. R. Kotamarthi,[2] O. J. Ogunsola,[1] L. W. Horowitz,[3] S. Walters,[4] D. J. Wuebbles,[1] M. A. Avery,[5] D. R. Blake,[6] E. V. Browell,[5] and G. W. Sachse[5]

Received 25 April 2001; revised 29 January 2002; accepted 31 January 2002; published 13 December 2002.

[1] Significant seasonal variations in the concentrations of several trace gases were observed in the southern tropical Pacific during the Pacific Exploratory Mission (PEM) TROPICS-A (PT-A, September/October 1996) and PEM TROPICS-B (PT-B, March/April 1999) campaigns. The objective of this study is to evaluate the relationship between the measured and modeled seasonal variabilities through comparisons of these observations with model calculations. A three-dimensional (3-D) global-scale chemical transport model was employed to (1) evaluate the seasonal variations in ozone and CO mixing ratios; (2) calculate an ozone budget and identify its controlling factors; (3) evaluate the effectiveness of atmospheric transport barriers in the model, such as the Intertropical Convergence Zone (ITCZ); and (4) test the sensitivity of ozone over the tropical south Pacific to biomass-burning emissions. The model reproduces the main features of the observed seasonal variation in ozone and CO. According to the model calculation, the ozone burden during the PT-A was larger due to the transport of ozone into the central pacific middle troposphere from the west, whereas a net outflow of ozone from this region to the east resulted in a reduction of ozone burden during the PT-B period. Transport of ozone from the Northern Hemisphere into this region was found to be much larger during the PT-B period compared with the PT-A period. The in situ production and loss of ozone calculated in the model agreed with that derived from measurements. The gradients in the model for selected trace gases across the ITCZ were shown to be qualitatively similar to measurements. *INDEX TERMS:* 0368 Atmospheric Composition and Structure: Troposphere—constituent transport and chemistry

Citation: Wei, C.-F., V. R. Kotamarthi, O. J. Ogunsola, L. W. Horowitz, S. Walters, D. J. Wuebbles, M. A. Avery, D. R. Blake, E. V. Browell, and G. W. Sachse, Seasonal variability of ozone mixing ratios and budgets in the tropical Southern Pacific: A GCTM perspective, *J. Geophys. Res.*, *107*, 8235, doi:10.1029/2001JD000772, 2002. [printed *108*(D2), 2003]

1. Introduction

[2] Ozone is a key component of smog and a useful indicator of the effects of trace gas emissions into the troposphere from anthropogenic and natural sources. The effects of anthropogenic emissions on atmospheric chemistry have been largely evaluated in terms of ozone changes [*NARSTO*, 1994]. The sources of ozone in the troposphere are the subsidence of stratospheric air and in situ chemical production; the sinks for tropospheric ozone are the physical removal at Earth's surface by dry deposition [*World Meteorological Organization* (*WMO*), 1995] and in situ chemical loss. Additionally, models constrained with measurements have shown that the net tendency from in situ chemistry is a small difference between large production and loss terms [*Davis et al.*, 1996; *Jacob et al.*, 1996]. This would mean that the gross production and loss terms are approximately in balance and small perturbations in the loss or production pathways of ozone can significantly affect the regional and global burden of ozone. Due to the importance of ozone in the chemistry of the atmosphere and its impact on air quality in general, it is necessary to understand the processes that control the formation, loss, transport, and burden of ozone in different regions of the atmosphere.

[3] The impact of anthropogenic emissions on atmospheric chemistry in different regions is currently under evaluation on the basis of limited observation data sets and modeling simulations. The main focus of the National Aeronautics and Space Administration's Pacific Exploratory Mission (NASA PEM) was to construct baseline measurements of trace gases and aerosols in selected remote locations over the Pacific from aircraft platforms and limited ground-level sampling [*Hoell et al.*, 1996, 1997, and 1999]. Data collected during these measurement campaigns provide a snapshot of the atmospheric conditions in these regions for limited time periods (typically 1 to 2 months). As a result, it is of importance to evaluate the

[1]Department of Atmospheric Sciences, University of Illinois, Urbana-Champaign, Illinois, USA.
[2]Argonne National Laboratory, Argonne, Illinois, USA.
[3]GFDL, Princeton, New Jersey, USA.
[4]NCAR, Boulder, Colorado, USA.
[5]NASA-Langley Research Center, Hampton, Virginia, USA.
[6]University of California-Irvine, Irvine, California, USA.

Copyright 2002 by the American Geophysical Union.
0148-0227/02/2001JD000772

relationship between the mean seasonal variability of the atmosphere and these limited data sets. This can be done by (1) extensive comparisons of the data sets to a few available results of long-term monitoring for a limited number of species, such as ozone and carbon monoxide, or (2) using global-scale chemical transport models to generate a chemical climatology of the atmosphere. To generate a "true" chemical climatology, the global-scale model needs to be run for several consecutive years and then the results averaged. This would be a formidable task with the current computational resources at our disposal. A medium term approach is to use meteorology generated from a GCM run designed to produce a "typical" year for the current climate. Here we applied the latter approach to evaluate the ozone budget in the southern tropical Pacific Ocean and compare the model results with measurements.

[4] The PEM-Tropics-A (PT-A) and PEM-Tropics-B (PT-B) field measurement experiments conducted by NASA under the Global Tropospheric Experiment (GTE) program provide a database of intensive measurements of ozone and its precursors in the tropical southern Pacific during two different periods of different years. PT-A was conducted during August–October 1996 (austral spring) [*Hoell et al.*, 1999]. Subsequently, PT-B was conducted during the austral fall period of March–April 1999 [*Raper et al.*, 2001].

[5] The South Pacific is the region of the tropical troposphere most remote from human activity. Investigating this region provides baseline data for gases that play a significant role in controlling the oxidizing power of the atmosphere, such as, ozone, H_2O, NO, CO, and nonmethane hydrocarbons (NMHCs). The timing of PT-A and PT-B corresponded to the dry and rainy seasons, respectively. *Schultz et al.* [1999] studied the ozone budget over the tropical South Pacific region with a global three-dimensional (3-D) model and a point model and suggested that the biomass-burning emissions in South America and Africa contributed to ozone over this region during PT-A.

[6] In this study we first examine and contrast the measured ozone mixing ratios during the PT-A period and the PT-B period with those calculated using a 3-D global-scale chemical transport model (GCTM). The focus of these comparisons is on aspects of the measurements that would be representative of a typical year in terms of meteorology. This is followed by an analysis of the sources and sinks of ozone in the South Pacific using a 3-D global-scale chemical transport model running off-line with dynamics generated by a climate model. The in situ ozone production and loss tendencies calculated by the 3-D GCTM are also compared with those calculated by a box model constrained with key measured trace gas mixing ratios and hence provide a close approximation of "measured" ozone production and loss rates. We also evaluate the calculated-ozone over the tropical South Pacific region through intensive comparisons with PT-A and PT-B measurements. In this process we examine the impacts of biomass burning from South America and Africa on tropospheric ozone in the middle of the Pacific Ocean. We also analyze the effectiveness of the model in representing transport barriers such as the Intertropical Convergence Zone (ITCZ) and the South Pacific Convergence Zone (SPCZ). No particular attempt is made, however, to evaluate specific processes in the model, which will be subjects of a later paper. The main features of ozone distribution, including seasonal variability and episodic elevations, are the subjects discussed in this paper.

2. Model Descriptions

[7] A global-scale 3-D chemistry transport model (GCTM), originally developed at National Center for Atmospheric Research (NCAR) and named MOZART (Model for Ozone and Related Trace gases) [*Brasseur et al.*, 1998; L. W. Horowitz et al., manuscript in preparation, 2002] was used to simulate the atmosphere with dynamical input fields from a climate model. The model results were then compared with the measurements from PT-A and PT-B to evaluate the model capabilities, such as, the ability to reproduce observed seasonal variability in trace gas distributions and the significance of transport barriers in the model compared to observations. A zero-dimensional (0-D) photochemical box model with a local equilibrium assumption was also used to calculate the production and loss tendencies of ozone and compared them with the results calculated from MOZART. Below is a brief description of these two models.

2.1. Three-Dimensional CTM

[8] The 3-D GCTM, MOZART (version 2, details are described by Horowitz et al., manuscript in preparation, 2002), has a horizontal resolution of 2.8° in latitude and longitude, and extends vertically from the surface to approximately 38 km. In the present study, we use a version of MOZART that is intermediate between version 1 [*Brasseur et al.*, 1998] and version 2 (Horowitz et al., manuscript in preparation, 2002). The GCTM has 34 vertical layers along hybrid sigma pressure coordinates with a vertical grid resolution varying from 60 meters near the surface to approximately 2 km at the top of the model domain. Transport is driven off-line by the middle atmosphere version of the NCAR Community Climate Model version 3 (MACCM3) with dynamical variables (wind fields, pressure, temperature, and convection) saved every 3 hours. The dynamical variables used in this version of MOZART were extracted from a long-term run of MACCM3 forced at the lower boundary with climatological values of sea surface temperatures (SST). This is expected to yield a representative year for the current atmosphere. It is in this sense that the MOZART results described below are referred to as "climatological." However, it should be noted that the MOZART results would be representative of the current climate, only if such factors as emissions are also "climatological" means. Since the emissions employed are from data sets built for a particular year, the simulation results presented here do not truly represent a chemical climatology.

[9] This model accounts for surface emissions (including N_2O, CH_4, CO, NO_x, NMHC, CH_2O, isoprene, acetone, etc.), chemical and photochemical reactions, advection, convection, and wet and dry deposition. The emission fluxes in MOZART for anthropogenic species were based on the Emission Database for Global Atmospheric Research (EDGAR) [*Olivier et al.*, 1996]. Horowitz et al. (manuscript

Table 1. List of Chemical Species Included in MOZART (Version 2)

No.	Species Name
1	$Ox = O(^3P) + O(^1D) + O_3$
2	N_2O
3	N
4	NO
5	NO_2
6	NO_3
7	HNO_3
8	HO_2NO_2
9	N_2O_5
10	CH_4
11	CH_3O_2
12	CH_3OOH
13	CH_2O
14	CO
15	OH
16	HO_2
17	H_2O_2
18	C_3H_6
19	Isoprene
20	$PO_2 = C_3H_6OHO_2$
21	CH_3CHO
22	$POOH = C_3H_6OHOOH$
23	CH_3CO_3
24	CH_3COOOH
25	$PAN = CH_3CO_3NO_2$
26	$ONIT = CH_3COCHO_2CH_2OHNO$
27	C_2H_6
28	C_2H_4
29	C_4H_{10} (surrogate for > = C_4 Hydrocarbons)
30	$MPAN = CH_2CCH_3CO_3NO_2$
31	$ISO1 = C_5H_9O_3$
32	$MVK = CH_2CHCOCH_3$
33	$MACR = CH_2CCH_3CHO$
34	$MOHO_2 = CH_3COCHO_2CH_2OH$
35	CH_2OHCHO
36	$MCO_3 = CH_2CCH_3CO_3$
37	$C_2H_5O_2$
38	C_2H_5OOH
39	$C_{10}H_{16}$ (α-pinene)
40	C_3H_8
41	$C_3H_7O_2$
42	C_3H_7OOH
43	CH_3COCH_3
44	$ROOH = CH_3COCH_2OOH$
45	$RO = CH_3COCH_2O$
46	$RO_2 = CH_3COCH_2O_2$
47	CH_3COCHO
48	Rn
49	Pb
50	H_2
51	O_3 Stratosphere
52	O_3 Inert

in preparation, 2002) presents a more detailed description of the emissions used in MOZART (version 2). The version of MOZART used here provides spatial and temporal distributions for 52 chemical tracers, as listed in Table 1, with a chemistry scheme similar to the one described by *Brasseur et al.* [1998] that incorporates 107 gas-phase, 5 heterogeneous, and 29 photochemical reactions. The empirical first-order heterogeneous reactions involving N_2O_5 and NO_3 on sulfate aerosols are implemented in the model (see *Müller and Brasseur* [1995] for details). Advection of the trace gases is simulated using the flux-form semi-Lagrangian (FFSL) formulation of *Lin and Rood* [1996] and replaces the previous shape-preserving semi-Lagrangian scheme [*Williamson and Rasch*, 1989]. The FFSL scheme is conservative and upstream biased. In addition, it contains monotonic constraints and conserves tracer correlations. Convective transport of trace gases is parameterized using the schemes developed by *Hack* [1994] for shallow convection and by *Zhang and McFarlane* [1995] for deep convection, as in CCM3. Vertical diffusion with the boundary layer is represented by the parameterization of *Holtslag and Bonville* [1993]. Dry deposition velocities for species (including O_3, NO_x, HNO_3, PAN, organic nitrates, H_2O_2, organic peroxides, CH_2O, CH_3COCHO, CO, CH_3COCH_3, CH_4, Pb-210) are computed from resistances specified as a sum of species) independent aerodynamic resistance and a species-dependent surface resistance. MOZART also contains wet deposition of soluble species (such as HNO_3, H_2O_2, CH_3OOH, C_3H_7OOH, C_3H_6OHOOH, CH_3CO-CH_2OOH, CH_3COOOH, C_2H_5OOH, HO_2NO_2, CH_3CO-CHO_2CH_2OHNO, CH_2O). For highly soluble gases (HNO_3 and H_2O_2), in-cloud scavenging and below-cloud scavenging by raindrops are included, as given by *Brasseur et al.* [1998]. In-cloud scavenging is parameterized for all other species according to *Giorgi and Chameides* [1985]. MOZART version 1 is described by *Brasseur et al.* [1998] and evaluated by *Hauglustaine et al.* [1998]. Horowitz et al. (manuscript in preparation, 2002) gives description and evaluation of MOZART version 2.

2.2. Photochemical Box Model

[10] The photochemical box model is based on the LLNL/UIUC 2-D zonal average model [e.g., *Patten et al.*, 2000]. The current version of this box model has 72 species, 132 thermal reactions, and 52 photolysis reactions. The model has full representation of CH_4, C_2H_6, and C_3H_8 chemistries, and condensed sets of reactions for isoprene, C_2H_4 and C_3H_6 [*Kotamarthi et al.*, 1999]. Heterogeneous chemistry including N_2O_5, $BrNO_3$ and $ClNO_3$ reactions on sulfate aerosol are included in the model. In addition, ClO_x, BrO_x, HO_x and NO_x chemistries [*DeMore et al.*, 1997] are simulated in the model. The photolysis rates are calculated by using a two-stream radiative transfer model with 128 bins for calculating absorption cross sections ranging from 170 to 450 nm [*Grant et al.*, 1987]. The chemical integrator employs the Gear method of *Hindmarsh* [1983].

[11] Box models are typically used to analyze data collected from aircraft platforms in either the equilibrium mode or the steady state mode. In the equilibrium mode, the model solves the equation

$$P_i = L_i n_i, \tag{1}$$

where P_i, ($cm^{-3}\ s^{-1}$) and L_i (s^{-1}) denote the photochemical production and loss frequencies for species i, whose concentration (cm^{-3}) is n_i. This approximation is valid for species with photochemical time constants of less than 1 hour, and it is similar to the approximation used for calculations in the PEM-West A and B missions [*Crawford et al.*, 1996; *Davis et al.*, 1996; *Kotamarthi et al.*, 1997].

[12] In calculating P_i and L_i, the concentrations of O_3, H_2O, CO, CH_4 and NO are fixed. The point-by-point calculations are used to calculate point-by-point NO_2 and HO_2 concentrations which are checked for consistency

against measurements, and then ozone production and loss tendencies are derived.

3. Numerical Experiments

[13] Three separate simulations were performed in the 3-D model. The first was a 1-year model simulation with daily outputs, an instantaneous value for 0 GMT and a diurnal average, of mixing ratios of all species, fluxes, and chemical tendency terms. The results from this run were then used to initialize two additional simulations, one for the August–September period (PT-A), and the other for the March–April period (PT-B). The outputs from these two limited-in-time simulations corresponding to the PT-A and PT-B periods were saved on an hourly basis in order to compare to the measurements made from the aircraft platform. In addition, the model recorded mixing ratios, mass fluxes across grid boundaries, chemical production and loss terms of trace gases at 0 GMT every day as the instantaneous values and the diurnally averaged values for the day. The photochemical box model was mainly used to calculate the photochemical production and loss tendencies of ozone with constraints on radiation and trace gas-mixing ratios from the PT-A and PT-B measurement data sets.

4. Results

4.1. Meteorological Conditions

[14] The PT-A period corresponded to the onset of a weak cold phase (La Niña) event in the tropical southern Pacific Sea Surface Temperatures (SST). *Fuelberg et al.* [1999] found only small variations in the assimilated wind fields for this period from an 11-year mean climatology. The deviations were found to be consistent with the onset of a weak La Niña episode. As a result, the PT-A period could be considered to mirror conditions close to a climatic mean state. However, the PT-B period coincided with the strongest phase of a La Niña event [*Fuelberg et al.*, 2001] which led to significant deviations of the assimilated wind fields from a 11-year mean climatology. Manifestations of these deviations include (1) a weaker than normal ITCZ, (2) the displacement of the SPCZ is to the west of its mean location, and (3) stronger-than-normal easterlies in the tropics. The combined effect of all these anomalies was expected to be a reduction in the strength of convection over the central Pacific [*Fuelberg et al.*, 2001].

[15] The MACCM3 meteorological data used in this study are from the long-term run using climatological mean SST as the driving boundary condition. The standard CCM3 model dynamic outputs were analyzed by *Hurrell et al.* [1998] and shown to give a reasonable agreement with the mean state of the atmosphere, with no significant biases in both hemispheres. Monthly averaged streamlines from MACCM3 of September and March for 1000-, 700-, 500-, and 300-mb levels, corresponding to the middle of PT-A and PT-B periods, respectively, are shown in Figures 1a and 1b. These streamlines characterize time-averaged large-scale flow patterns during the PT-A and PT-B periods. The patterns and main circulation features of these streamlines are very similar to those derived from European Center for Medium-Range Weather Forecasts (ECMWF) reanalysis data sets [*Fuelberg et al.*, 1999, 2001]. However, some specific aspects of the flow, such as the locations of anticyclones in the eastern half of the Southern Hemisphere are not exactly at the same locations as compared with the reanalysis data [*Fuelberg et al.*, 1999, 2001]. This was noted as an anomaly for the PT-B period due to the occurrence of the La Niña event [*Fuelberg et al.*, 2001].

[16] Other important circulation systems near the surface that can be observed in the streamline maps are the ITCZ and the SPCZ. The ITCZ is a narrow low-latitude zone in which air masses originating in the northern and southern hemispheres converge and generally produce cloudy, showery weather. Over the Atlantic and Pacific it is the boundary between the northeasterly and southeasterly trade winds. The mean position of the ITCZ is somewhat north of the equator, but over the continents its location varies considerably. The locations of the ITCZ derived from the climatological model for the PT-A period and PT-B period (Figures 1a and 1b) are approximately the same as those recorded for the same periods [*Fuelberg et al.*, 1999; 2001]. On the other hand, the SPCZ is an atmospheric convergence zone in the southwestern Pacific Ocean that is characterized more by a convergence in wind direction than as a wind speed minimum. It extends from east of Papua New Guinea in a southeastward direction toward 120°E and 30°S. The SPCZ does not appear to have counterparts in the Northern Hemisphere. Though the SPCZ can be inferred from the MACCM3 results, the SPCZ for the PT-A period (Figure 1a) is much weaker in CCM3, and a few degrees east of those reported by *Fuelberg et al.* [1999]. For the PT-B period, *Fuelberg et al.* [2001] reported that the SPCZ was not as well defined as it was during the PT-A period. The MACCM3 derived streamlines (Figures 1a and 1b) have similar seasonal variation in the SPCZ. In addition, the convergence zone at the 1000-mb level during the PT-B period in the southern Pacific is a few degrees to the west as compared with the PT-A period. The convergence zone is not evident at the 700-mb level and higher during the PT-B period (Figure 1b), whereas during the PT-A period it is evident up to 500 mb (Figure 1a).

[17] We further analyzed the differences between the MACCM3 wind fields and those from the reanalysis wind fields from the National Center for Environmental Prediction (NCEP) for the years 1996 and 1998. This leads to similar conclusions as of *Fuelberg et al.* [1999, 2001] analysis, mainly that the wind fields are in general similar to a climatological mean with some exceptions. We also find that for both the periods simulated in this study, the surface winds from MACCM3 differ from those of NCEP by between 2 to 5 m/s in much of southern central tropical Pacific. The easterly wind between 10°N and 10°S is weaker in the MACCM3 by 5 m/s at 700 mb and decreases to between 2 and 5 m/s at 500 mb and is negligible at 200 mb, for the month of March. The nearly zonal flow from west to east beyond 30°S is stronger in the MACCM3 by about 5 m/s above 500 mb. A similar situation was found for the month of September, with differences between the wind fields being smaller than in March.

[18] In summary, the main differences in meteorology between the PT-A and PT-B is the location and strength of the ITCZ and the SPCZ. The main seasonal difference in the ITCZ is the movement of the ITCZ from 10°N during PT-A to near 5°S during PT-B. As discussed above, the wind fields of 1000 mb from MACCM3 showed similar but a

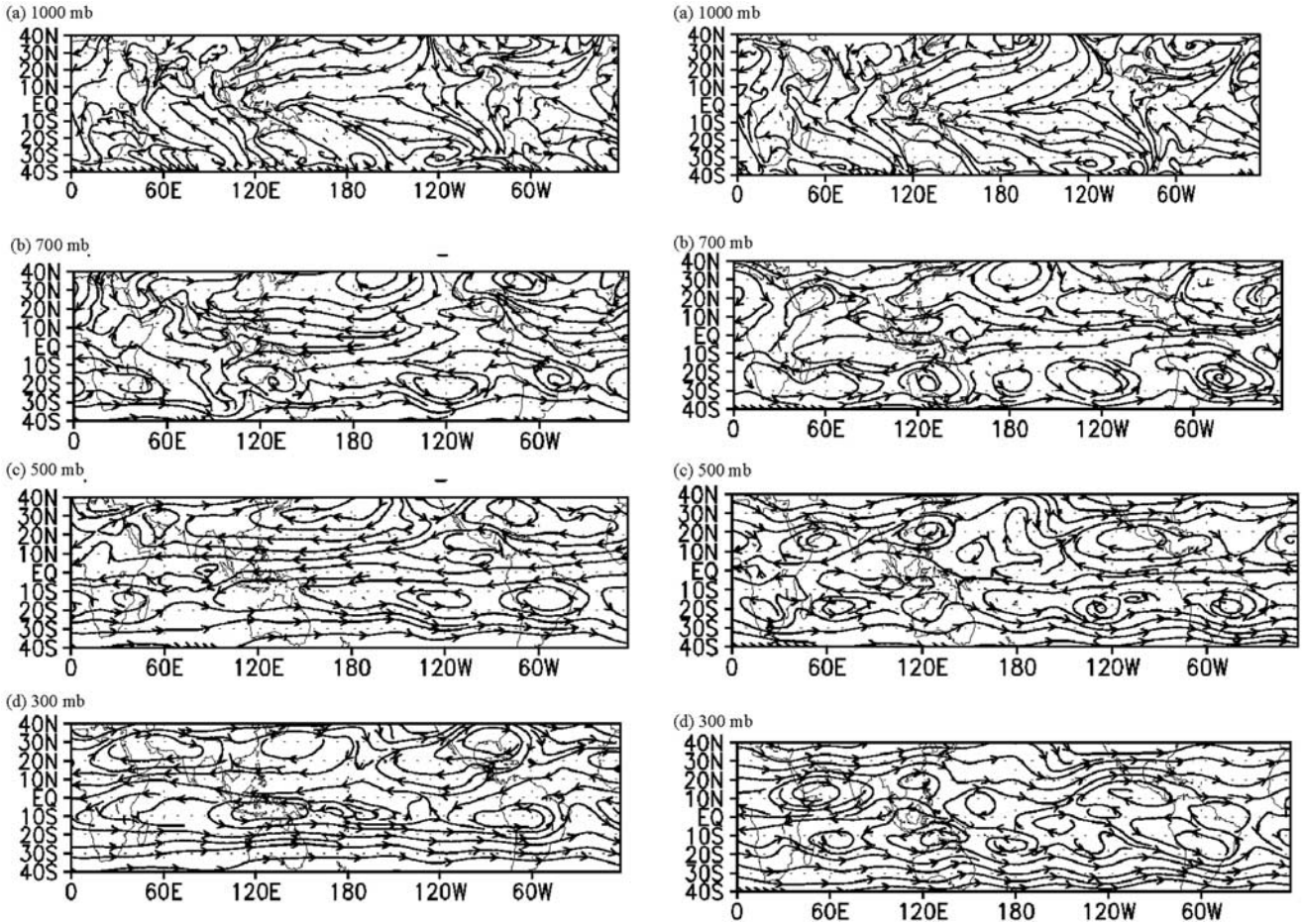

Figure 1. (a) Mean streamlines for September from CCM3 output used by the dynamical driver in MOZART (v2). The figure shows streamlines for four different pressure levels. (b) Mean streamlines for March from CCM3 output used by the dynamical driver in MOZART (v2). The figure shows streamlines for four different pressure levels.

smaller shift for the ITCZ. The second major feature was the stronger SPCZ and its more eastward location during PT-A than PT-B. The MACCM3 dynamic fields have a weak SPCZ during both these periods, but are able to capture the shift in its location from March to September. Thus given the general agreement between the wind fields used in the model and observed for this period we should expect the modeled and measurement comparisons for ozone and other trace gas to be reasonably free of differences in the dynamical fields.

4.2. SHADOZ Comparison

[19] Ozonesonde data were collected in the southern tropics over a 2- to 3-year period under the Southern Hemisphere Additional Ozonesondes (SHADOZ) program to coincide with the PEM-Tropics field measurement program [*Thompson and Witte*, 1999]. Figures 2a and 2b are the austral fall and spring monthly averages of ozone profiles plotted from the model and measurements for Fiji (−18.13°S, 178.40°E) and for the austral spring in Tahiti (18°S, −149.00°E). A typical data point from the SHADOZ sites in these figures is an average of eight data points resulting from four launches in a month for the years 1998 and 1999. In order to compare with the ozonesonde data, diurnal average ozone mixing ratios were extracted from a 1-year simulation of MOZART with daily outputs of mixing ratios (listed in Table 1). Consequently, the data point at each altitude from MOZART is the mean value and standard deviation of the 30-day diurnally averaged ozone mixing ratios for the respective months. In Figure 2a, the best agreement between the model and measurements occurs during September in Fiji. For the rest of the 3 months shown, the largest discrepancy occurs in the midtroposphere. The model underestimates ozone by 10 $\sim$ 20 ppb in the midtroposphere in Fiji during March and April (Figure 2a). The relatively high ozone mixing ratios in the midtroposphere is one of the salient features of the PT-A period, and possible reasons for this mid tropospheric increase in ozone are discussed in section 4.3. Note that there were not sufficient data for the months of March and April from Tahiti for similar comparisons. For September the measurements and the model at Tahiti (Figure 2b) are in good agreement, with differences of less than 5 ppb, through the tropospheric column. The measured ozone for October at Tahiti is less than the modeled ozone in the midtroposphere by about 10 ppb. The MOZART profiles above 300 mb in Figure 2b suggest that the model is experiencing higher ozone subsidence in this region com-

a.

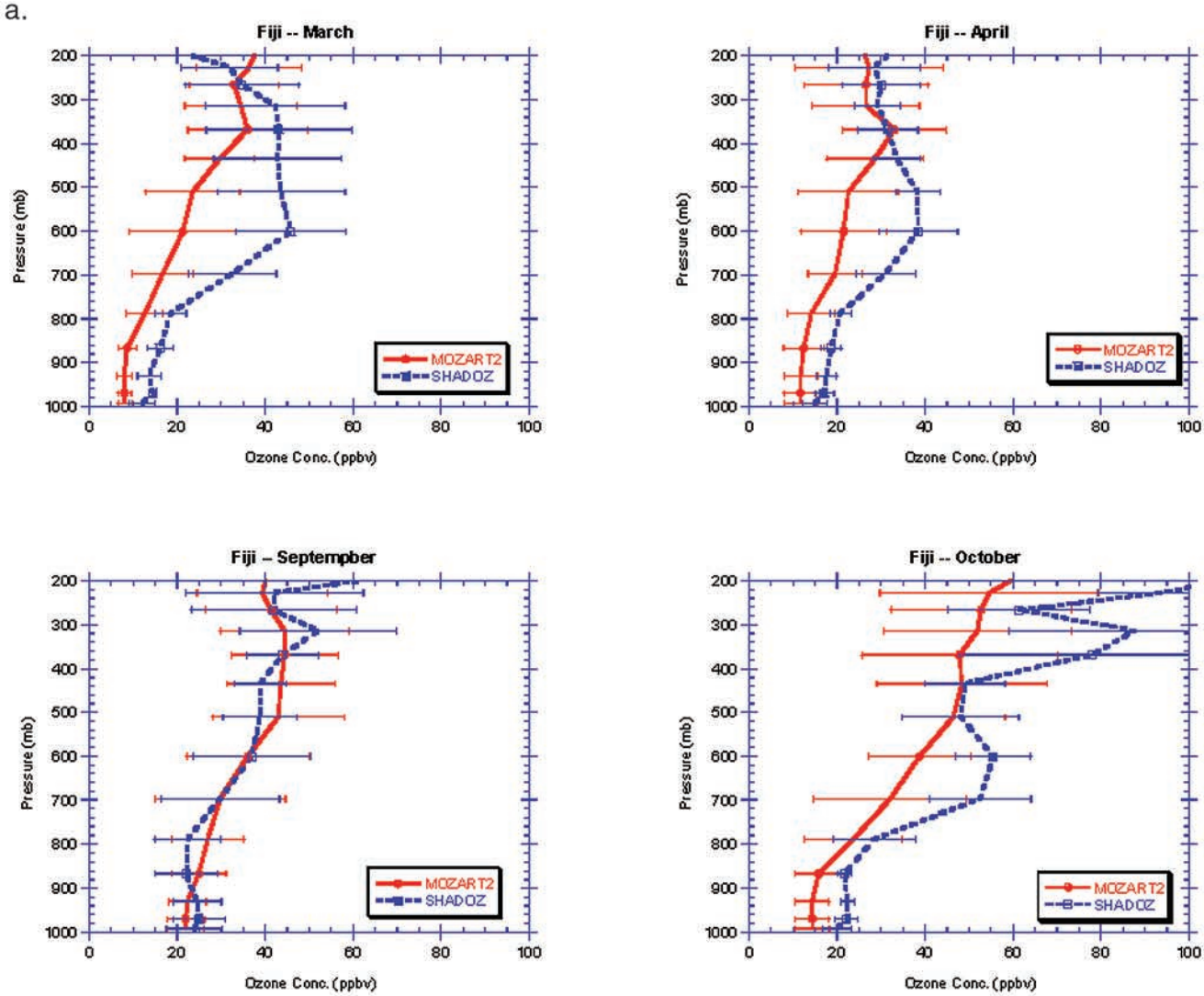
Fiji -- March
Fiji -- April
Fiji -- September
Fiji -- October
Pressure (mb)
Ozone Conc. (ppbv)
MOZART2
SHADOZ

b.

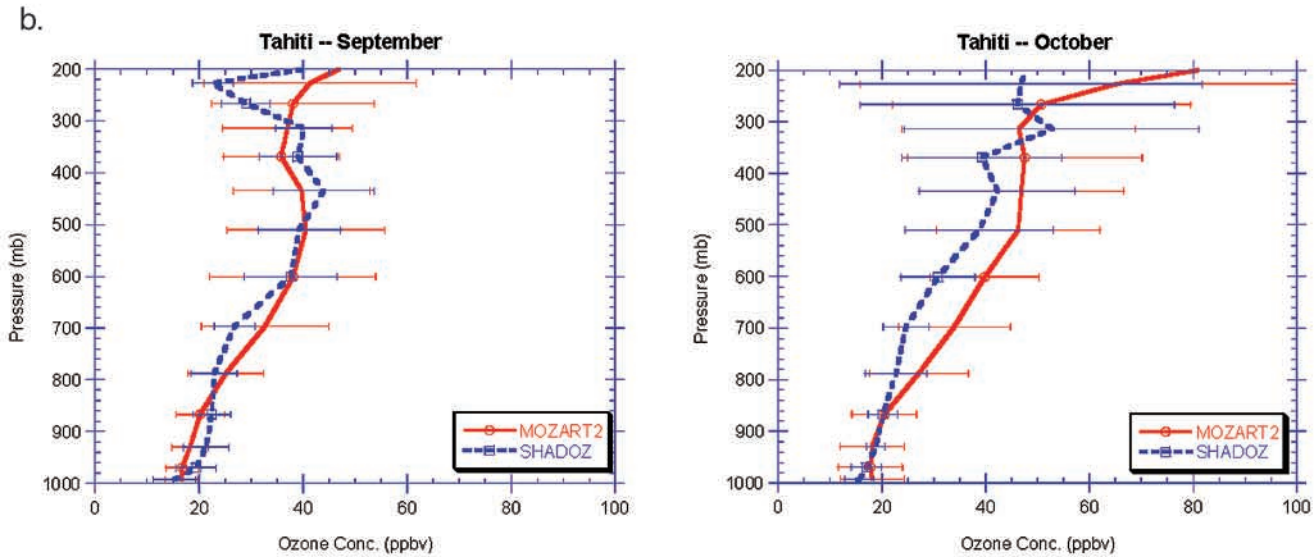
Tahiti -- September
Tahiti -- October
Pressure (mb)
Ozone Conc. (ppbv)
MOZART2
SHADOZ

pared with the observations. This results from a lower-than-observed height of the tropopause in the model during this period over this region, as further discussed in section 4.4.

4.3. Ozone and CO Comparisons

[20] Ozone and CO measured during the PT-A and PT-B periods were compared with model results for evaluating seasonal variations. The measurements for the PT-A and PT-B period from the DC-8 platform were from a 1-minute average, merged data file generated by the atmospheric chemistry research group at Harvard University. The MOZART model used results from a simulation, which saved results once every hour for the respective months. These calculations were initialized with output from a 1-year calculation, which saved model results once every day. Additionally, each of the simulations for the PT-A and PT-B period had 1-month spin up. For example, the model results shown here for September, were initialized on 1 August using the 0 GMT output from the 1-year run and then the model calculations continued to the end of September, with model results saved every hour for this entire 2-month period. Results from these limited-in-time simulations corresponding to the PT-A and PT-B periods, saved every hour, were used to compare to observations. Figure 3a displays all of the ozone data collected during the PT-B period from 30°S to 30°N in latitude and from surface to 12 km [*Avery et al.*, 2001]. If several ozone measurements were made in a particular altitude-latitude bin, the average of these values was plotted. Each of the data points extracted from MOZART is the closest in time and location to the measurements. Since the model saves only hourly outputs and on a coarser spatial grid than the observations, the closest point to the observations selected from the model often corresponds to several measured data points. This procedure is used repeatedly to extract model results for the 2-month period corresponding to each experiment and then averaged to obtain the figures presented below. Figure 3b shows the model-calculated ozone sampled at the same locations and times (the closest model grid and time) corresponding to the measurements and averaged for March and April, plotted using the same procedure as in Figure 3a. In general, the model reproduces the very low concentration of ozone observed in the tropical Southern Hemisphere. The differences in the measured and model simulated ozone for the PT-B period are shown in Figure 3c. There are only a few ppb differences from 5°N to 25°N in the lower troposphere (0–2 km). However, the elevated ozone observed in the tropical Northern Hemisphere is shifted north in the model. In addition, the model cannot capture a few pockets of elevated ozone observed at 10–12 km. These pockets of high ozone represent episodes of long-range transport of ozone from East Asia to the northern tropical Pacific and possibly from South Africa or South America to the extra-tropical regions of the South Pacific [*Maloney et al.*, 2001]. The model generally underestimates ozone by 10 ppb or more in the midtroposphere which is similar to the differences seen in the SHADOZ comparison in Fiji (Figure 2a).

[21] A similar set of ozone comparisons for the PT-A period is shown in Figures 4a [*Gregory et al.*, 1999], 4b, and 4c. The main feature of the PT-A data set is the incident of elevated ozone in the mid-to-upper troposphere (6 km and above) in the southern tropics as shown in Figure 4a. The derived ozone mixing ratios from model calculations at 4 km and above between 25° to 15°S (Figure 4b) are less significantly elevated than the ones observed in the data set (Figures 4a and 4c) by more than 10 ppbv. This might be due to the under representation of biomass-burning emissions in the GCTM at the southern tip of Africa, which is assumed to be the major source for elevated ozone [*Fuelberg et al.*, 1999]. Another possible reason is that the GCM fields may not represent well a specific meteorological event or condition during or prior to the PT-A sampling period. However, a quick review of the meteorological conditions reported by *Fuelberg et al.* [1999] indicated a particularly strong subtropical jet, but no other extraordinary features were reported compared to climatology. A close examination of Figure 4c also reveals pockets of high ozone calculated by the model close to this region (4 to 6 km). This would suggest that transport in the model is occurring at slightly lower altitudes than measured.

[22] Since CO can be produced through incomplete combustion and is an indicator of biomass/anthropogenic influence on air masses [*Blake et al*, 1999], we performed an analysis for CO similar to that for ozone. Figures 5a and 5b represent the distribution of CO mixing ratios from the measurements (N. S. Pougatchev et al., CO during PEM-Tropics B mission, submitted to *Journal of Geophysical Research*, 2002) and model calculations for PT-B, and Figure 5c is the difference. The agreement is generally excellent between the modeled and measured CO for this period, with differences of less than a few ppbv throughout much of the region. The model in general is biased toward underprediction between 10°S and 30°S. The measured CO was higher than calculated by the model in the region between the equator and 10°S and below 6 km at 20°N. For the PT-A period CO was found to be elevated throughout much of the mid troposphere, between 15°S and 25°S and around 45°S (Figure 6a). This region of higher CO corresponds to the measurements of high ozone (Figure 4a). The model results also show elevated CO in this region of the Southern Hemisphere (Figure 6b). However, the difference between the measured and modeled CO is often in excess of 20 ppbv (Figure 6c). The reasons for these discrepancies are similar to those discussed for ozone.

[23] In summary, the ozone and CO during the PT-A period, in general, was higher than measured during the PT-B period. The model produces the same seasonal behavior in the abundance of these gases in this region as observed,

Figure 2. (opposite) (a) Monthly mean and standard deviation of SHADOZ ozonesonde profiles for the PT-A (September, October) and PT-B (March, April) time periods, compared with MOZART (v2) calculations at Fiji (−18.13°S, 178.40°E). SHADOZ data is from weekly ozonesonde releases over a 2-year period. MOZART (v2) results represent the mean and standard deviation of diurnal average values of ozone for each day of the respective month. (b) Monthly mean and standard deviation of SHADOZ ozonesonde profiles for the PT-A (September, October) time period, compared with MOZART (v2) values at Tahiti (−18°S, −149°E). Other details are as described for (a).

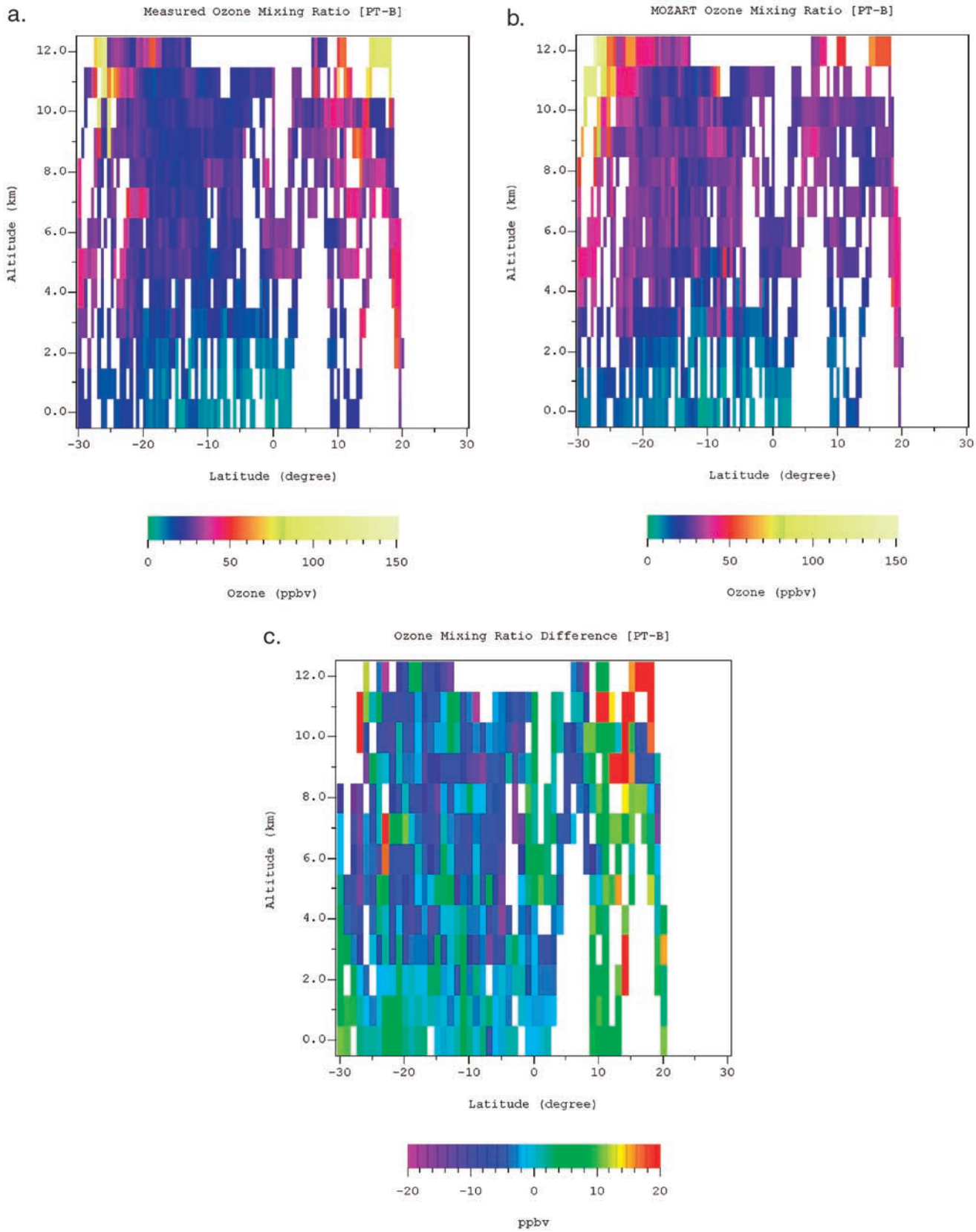

Figure 3. (a) Measured ozone from all DC-8 flights during PT-B. All point measurements of ozone are shown, except that if several measurements exist in a given altitude, latitude bin, the average ozone for that bin is plotted. (b) MOZART (v2) calculated ozone (average) for March and April (PT-B), sampled at the nearest spatial location and at local time, with measurements shown as in (a). (c) Absolute difference between measured and modeled ozone (a–b) for the PT-B time period.

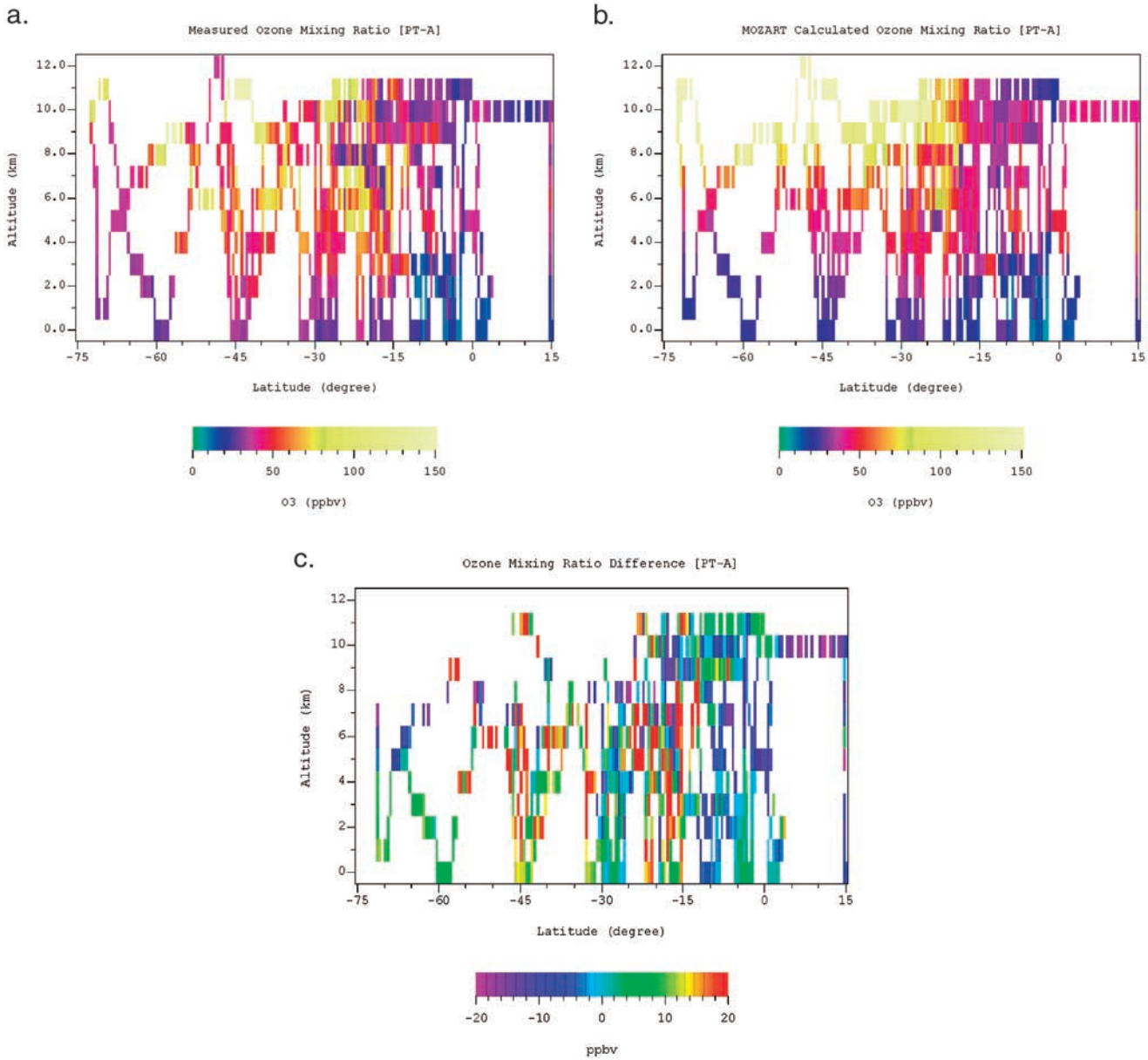

Figure 4. (a) Measured ozone from all DC-8 flights during PT-A. All point measurements of ozone are shown, except that if several measurements exist in a given altitude, latitude bin, the average ozone for that bin is plotted. (b) MOZART (v2) calculated ozone (average) for PT-A, sampled at the nearest spatial location and at local time, with measurements shown as in (a). (c) Absolute difference between measured and modeled ozone (a and b) for the PT-A time period.

higher values during the PT-A period compared with the PT-B period, but has a tendency for under predicting ozone in this region for both periods. Elevations of the mixing ratios of these gases in certain pockets of air could be a result of episodic long-range transport which were not reproduced in the model.

4.3.1. Sensitivity of Biomass-Burning Emissions From South Africa and Southern America

[24] PEM-Tropics-A was conducted at the end of the dry season in the southern tropics, when considerable biomass burning is known to take place [*Olson, et al.*, 1999]. *Staudt et al.* [2002] have argued that the sources of biomass burning affecting ozone and aerosols over the South Pacific are primarily from agricultural and forest fires in South America and southern Africa. In contrast, the counterpart of PEM-Tropics-B was conducted during the dry season of the northern tropics and an exceedingly clean atmosphere over the South Pacific.

[25] Analyses of fire counts observed by satellite indicated that the emissions during September 1996 were not substantially different from the long-term mean [*Olson et al.*, 1999]. We therefore used climatological biomass-burning emissions described by *Brasseur et al.* [1998] with some adjustments to account for more recent data (Horowitz et al., manuscript in preparation, 2002). Table 2 shows the global emissions for each chemical compound, including biomass-burning sources. However, as discussed in section 4.3, the concentration of O_3 and CO in the midtroposphere over the

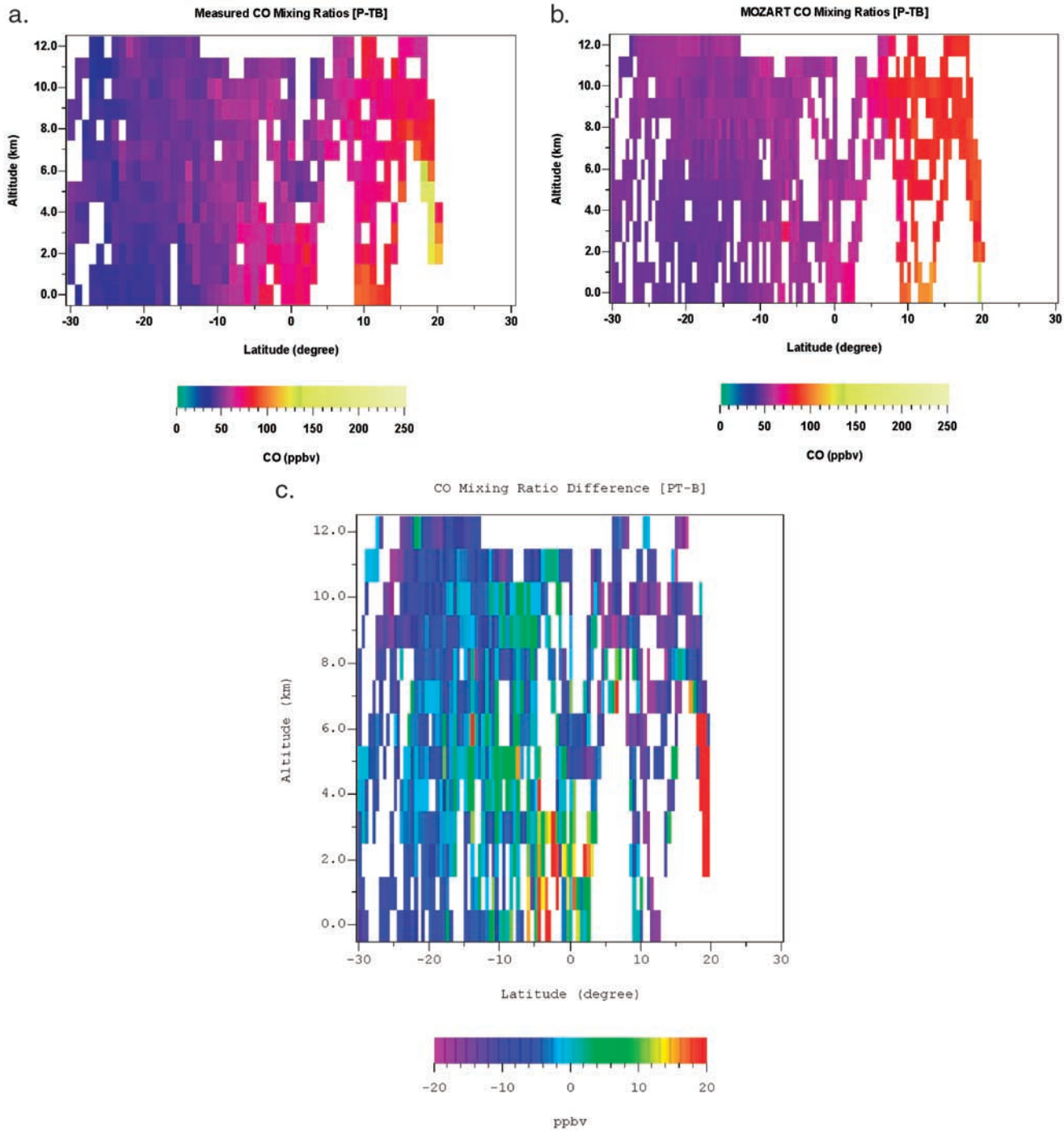

Figure 5. (a) Measured CO from all DC-8 flights during PT-B. All point measurements of ozone are shown, except that if several measurements exist in a given altitude, latitude bin, the average CO for that bin is plotted. (b) MOZART (v2) calculated CO (average) for March and April (PT-B), sampled at the nearest spatial location and at local time, with measurements shown as in (a). (c) Absolute difference between measured and modeled CO (a and b) for the PT-B time period.

southern tropical Pacific was lower in the model compared with observations for the PT-A period. The lower concentrations of ozone and CO in the model could be due, in part, to under representation of biomass-burning emissions in the model.

[26] To test the sensitivity of the modeled ozone concentrations to biomass-burning sources, we performed two additional simulations for the PT-A period other than those described in the above numerical experiments. For the first test case, the biomass-burning emissions (including NO_x and CO) were doubled only over South Africa (from 15°S to the tip of Africa) in the model. For the second test case, the biomass emissions were doubled only over South America (from the equator to the tip of the continent),

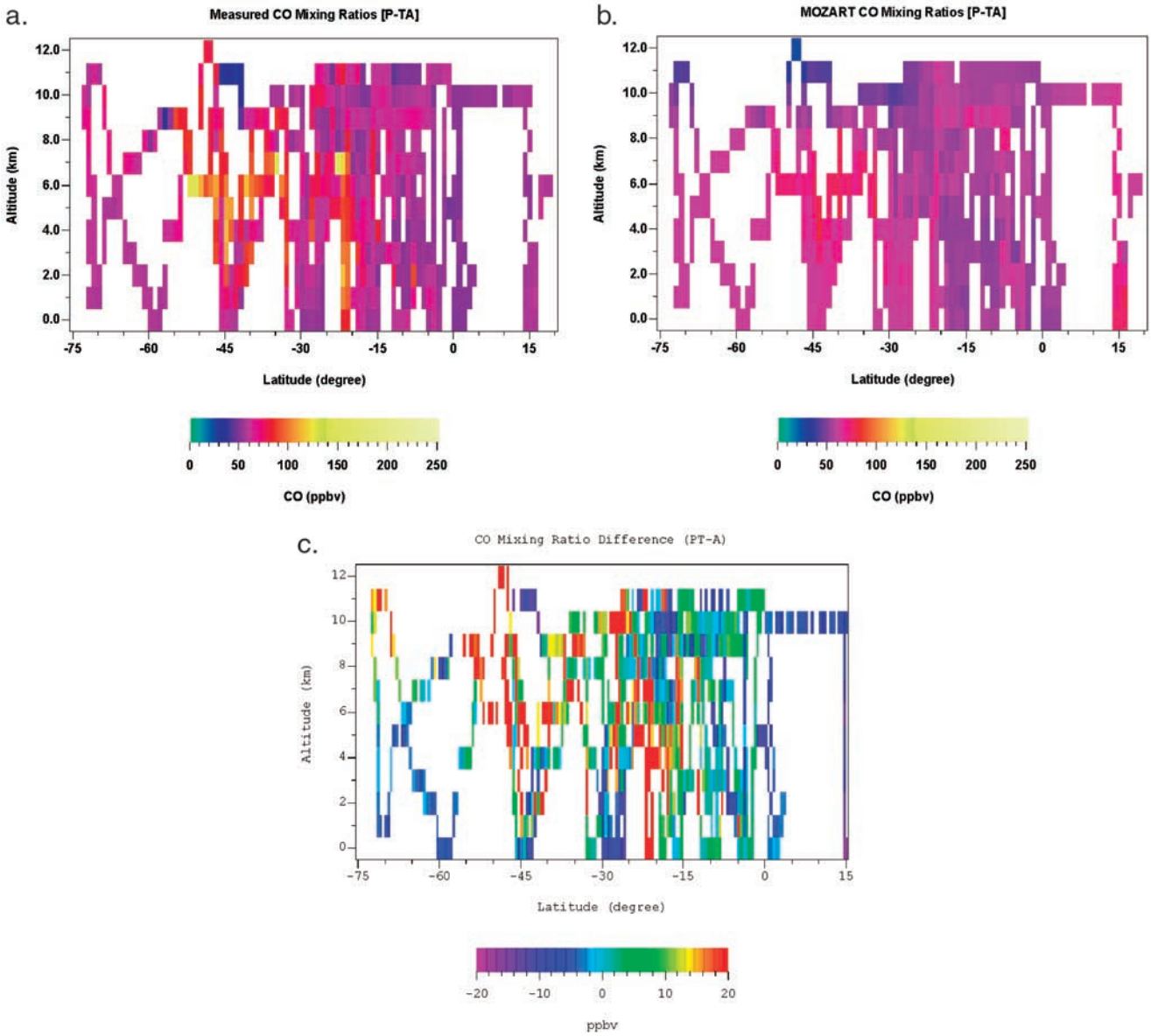

Figure 6. (a) Measured CO from all DC-8 flights during PT-A. All point measurements of ozone are shown, except that if several measurements exist in a given altitude, latitude bin, the average CO for that bin is plotted. (b) MOZART (v2) calculated CO (average) for PT-A, sampled at the nearest spatial location and at local time, with measurements shown as in (a). (c) Absolute difference between measured and modeled CO (a and b) for the PT-A time period.

and the emissions from South Africa were set back to the value used for the standard model simulation.

[27] The ozone change from the case where biomass burning in the southern Africa was doubled to the base case is shown in Figure 7a. The increase in ozone at 15°S to 25°S in the midtroposphere is in the range of 2 ppbv, but an increase of more than 10 ppbv at 30°S was calculated in the upper troposphere. These locations corresponded to the region where increased ozone was observed during the PT-A period as shown in Figure 4a. The counterpart analysis for ozone change with doubled biomass emissions in South America is plotted in Figure 7b. The increase in ozone for this case at 15°S to 25°S is over 2 ppb, and the peak ozone increase in the upper troposphere near 30°S is between 10 and 20 ppb, larger than that for the first case. In both cases, the ozone increases in the similar regions with similar strengths. Since the model is sensitive to the amount of biomass-burning emissions in both southern Africa and S. America, it is difficult to determine which location of the biomass burning is the major cause for the ozone increases during the PT-A period. Our calculations suggest that biomass-burning sources in either region investigated could have contributed to the observed midtropospheric ozone in the 15°S to 30°S region.

[28] The PT-A measurements (Figure 6a) reveal an increase in CO over a broad area from 15°S to 50°S in the midtroposphere, but the MOZART model shows a small uniform increase of CO in this area from the surface to the

Table 2. Global Surface Emissions of Source Gases in MOZART (Version 2)[a]

Species	Total	Forest Burning	Savannah Burning	Fuel Wood Burning	Agriculture Waste	Soil	Fossil Fuel
NOx, TgN/yr	35.47	2.43	4.08	0.32	0.67	6.61	21.36
CO, Tg/yr	1218.96	297.20	206.83	97.51	61.05	162.04	381.33
CH_4, Tg/yr	470.09						
CH_2O, Tg/yr	2.33						
C_3H_6, TgC/yr	18.50						
C_2H_4, TgC/yr	30.32						
C_2H_6, TgC/yr	11.91						
C_4H_{10}, TgC/yr	206.52						
C_3H_8, TgC/yr	9.19						
Acetone, Tg/yr	18.51						
Isoprene, TgC/yr	220.114						
Terpene, TgC/yr	129.59						
N_2O, TgN/yr	2.31						

[a]Emissions are in units listed next to the respective species.

upper troposphere. However, the increasing CO resulting from doubling biomass emissions from South Africa is concentrated in the 6km to 8km altitude at 30°S to 45°S (Figure 8a). The same calculation performed for doubling biomass emissions in South America gave results more consistent with the observations, with increases concentrated in the midtroposphere (4 km to 6 km) and approximately at 15°S to 50°S (Figure 8b). Therefore, the cause for the CO increases during PT-A is likely due to the biomass burning from South America.

[29] If we use CO as an indicator for biomass burning, the model calculations suggest that increased biomass burning from South America is the cause for the observed midtropospheric elevations of CO during the PT-A period. The ozone calculations are less conclusive and show no preference to sources from either South America or South Africa. Ozone calculations are sensitive to initial conditions inside the biomass-burning plume for such trace gases as nonmethane hydrocarbons and NO_x, whereas the CO mixing ratios depend significantly more on its emission strength and

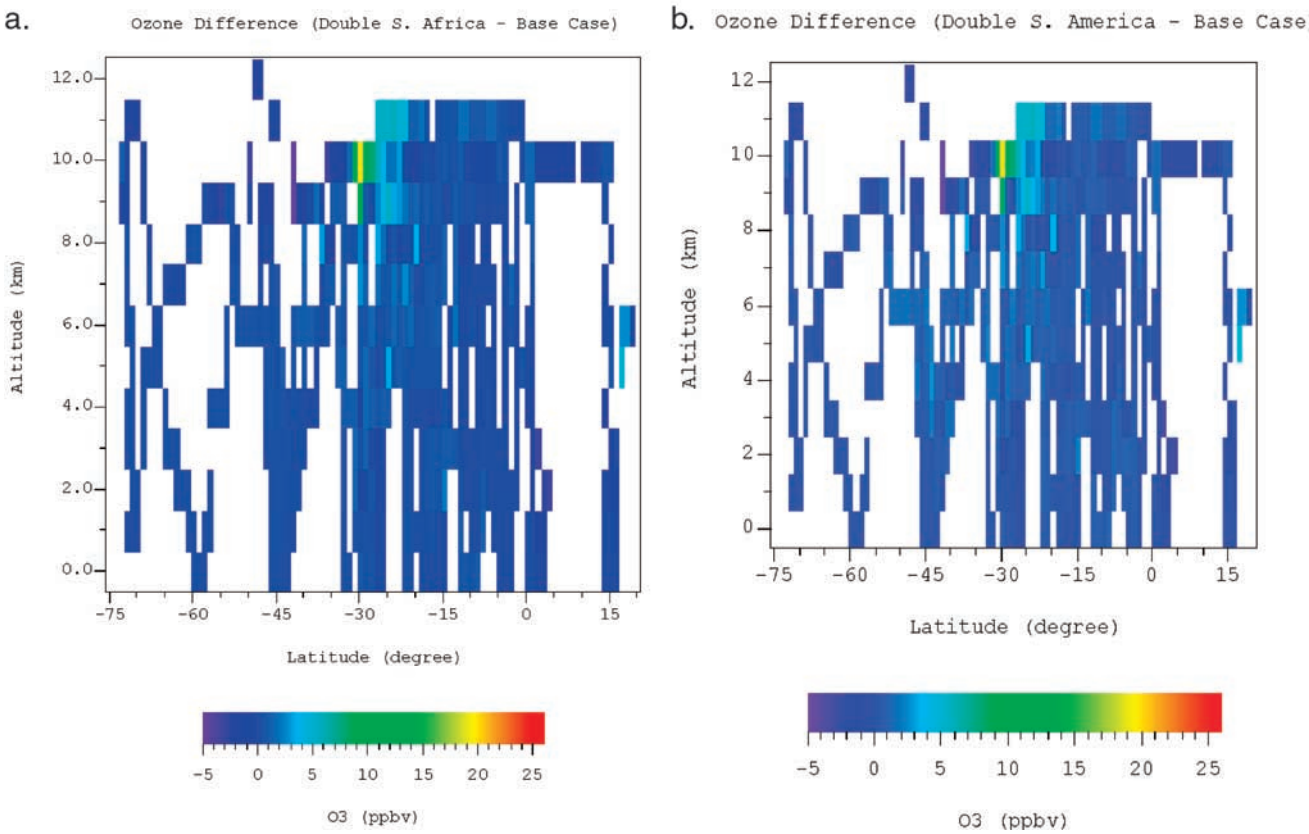

Figure 7. (a) Ozone difference for a case with doubled biomass-burning emissions over South Africa and for the model calculation with the standard emissions. (b) Ozone difference for a case with doubled biomass-burning emissions over South America (all locations south of the equator) and for the model calculation with standard emissions.

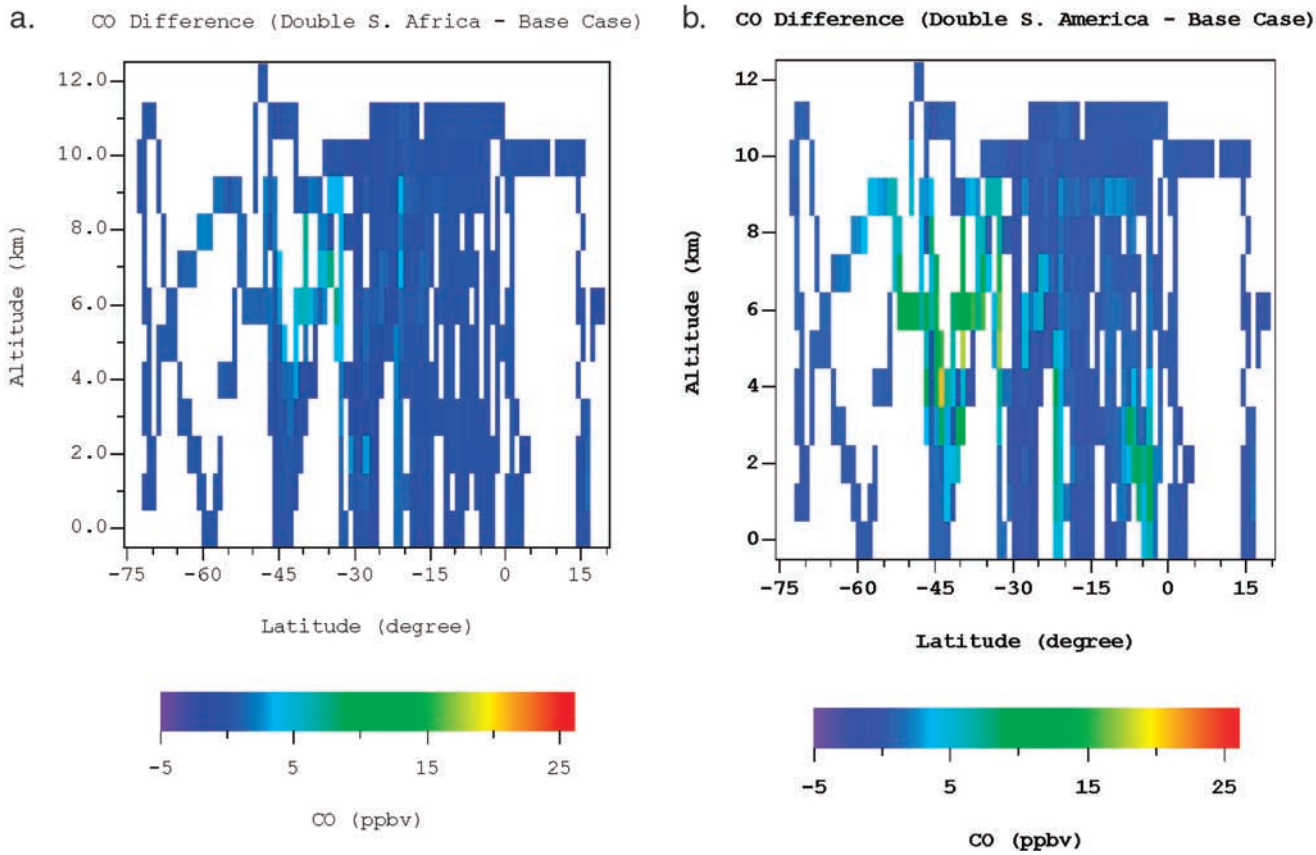

Figure 8. (a) CO difference for a case with doubled biomass-burning emissions over South Africa and for the model calculation with standard emissions. (b) CO difference for a case with doubled biomass-burning emissions over South America (all locations south of the equator) and for the model calculation with standard emissions.

transport time from the source to the receptor. The long distance from the source to the receptor location would require the use of a tracer of biomass burning both in the measurements and the model to further address this issue. Thus, the limited sensitivity studies performed here indicate the possibility of an underestimate of biomass-burning emissions in the Southern Hemisphere. However, with this current set of calculations we are unable to identify which region (i.e., South America or South Africa) contributes to this underestimate in the emissions.

4.4. Comparison With Lidar Ozone Data

[30] The investigations of O_3 and aerosols conducted with a DIfferential Absorption Lidar (DIAL) system as part of PEM-Tropics field experiments focused on the chemistry and transport of O_3 and aerosols in a wide range of tropospheric environments. Lidar measures ozone from near the surface to above the tropopause along the flight track of each DC-8 flight during both the PT-A and PT-B periods [*Fenn et al.*, 1999; *Browell et al.*, 2001]. These measurements provided the distribution of ozone concentrations in the column along the path of the flight. They provide further insights into the causes of elevated ozone layers due to the ability to measure the thickness of these layers and their connections to ozone rich regions of the atmosphere, such as the stratosphere. Figure 9 is a plot of the mean measured values of ozone for the PT-A and PT-B periods, averaged over the longitudes and latitudes along all the flight tracks [*Browell et al.*, 2001]. The longitude and latitude and time locations along the flight tracks were used to sample the ozone through the column in the model and then averaged over the respective 2-month periods. The model results used for this analysis are also from the limited-in-time runs as discussed in the previous section. Figures 10b and 10d are the latitudinal averages of these ozone profiles from the model and Figures 10a and 10c are longitudinal averages over each model latitude grid point, as shown in the plot. Several features can be noticed by comparing model results with the lidar data (Figure 9). In the MOZART latitudinal distribution plot (Figure 10a), the tropopause derived from the model is lower in the Northern Hemisphere (NH) than the lidar measurements indicate. The higher ozone values in the NH (beyond ~15°N) from the surface to the tropopause level are represented in the model. The model simulated well the low values of ozone at 0–2 km extending from 10°N to 40°S, whereas the measurements show higher ozone levels from 25°S to 40°S at these altitudes. The higher ozone values from 4 km to the tropopause from 30°S to 40°S are indicative of stratospheric subsidence both in the model calculation and measurements. The low ozone

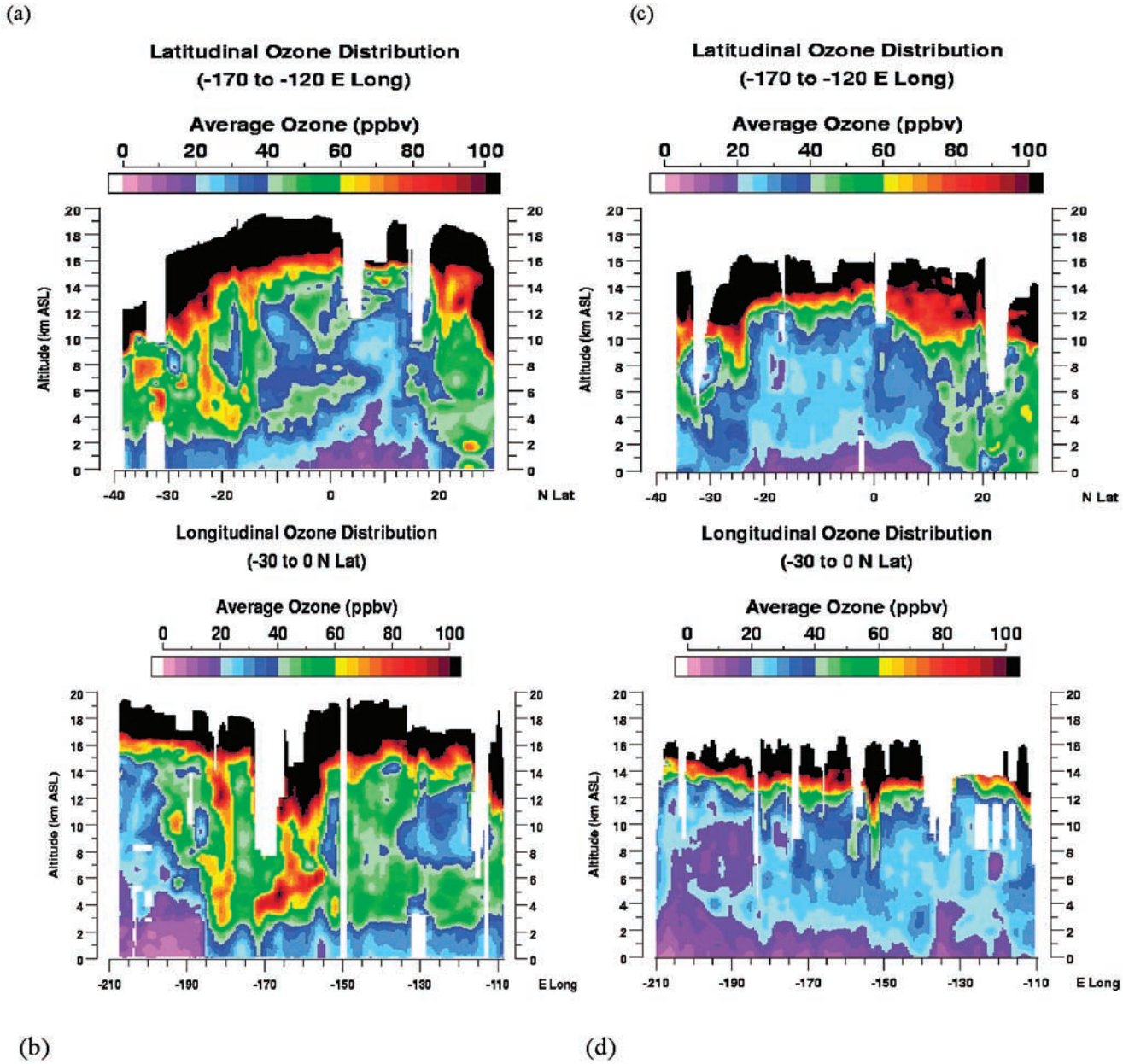

Figure 9. Averaged ozone profiles as a function of latitude (a, c) and longitude (b, d) from lidar measurements for the PT-A (a, b) and PT-B (c, d) time periods, as reported by *Browell et al.* [2001].

extending from 20°S to 10°S at 8–10 km in MOZART is also found in the measurements, though in a much smaller region.

[31] A decrease in the tropopause height from the east to west appears in the model (Figure 10b), as well as in the lidar data set (Figure 9). A layer of low ozone extends from east to west and the thickness of this layer decreases from surface to 4 km at the eastern edge to 2 km on the western edge in both the measurements and model calculations. Other low ozone regions measured by the lidar at approximately −200°east longitude and −130°east longitude in the mid-upper troposphere are also present in the model, though the ozone values are almost 10 ppb higher than the measured values.

[32] These results suggest that the measured ozone values during the PT-B period are in general agreement with predictions from MOZART (v2), a GCTM operating with dynamics derived from a climate model. As a result, the measurements appear nearly representative of the ozone climatology for this region and this particular period of the year, at least to the extent that the model can be regarded as representative of the climatology.

[33] A similar analysis was carried out for the PT-A period. Figure 10c shows the latitudinal distribution of ozone for this period from the MOZART model. The region with lowest levels of ozone is centered at 5°N and extends from 0 km to 2 km in both the model and lidar data set. The stratosphere in the model is lower during this period than in

the PT-A period and occurs at approximately the same location in the model as in the data set. Low ozone extends throughout the middle and upper troposphere from 20°S to 10°N in the model and is similar to the lidar data set. However, the localized increase in ozone observed in the middle and upper troposphere in the lidar data set from approximately 20°S to 40°S is much more diffuse in the model, with no increases in localized pockets disconnected from the stratosphere.

[34] Figure 10d, the longitudinal distribution of ozone for the PT-A period from the MOZART model, shows the lowest levels of ozone occur on the eastern edge in the layer at 0–2 km. The ozone-mixing ratio increases in this layer to over 20 ppb and reaches 30 ppb at the western edge of the plot. A similar behavior is observed in the lidar data (Figure 9). The layers of high ozone in the middle and upper troposphere observed in the lidar data are not reproduced in the model; rather the model exhibits an almost uniform increase in ozone mixing ratios with altitude from east to west. The western edge of Figure 10d shows low ozone mixing ratios extending deeper into the midtroposphere than at the eastern edge, a feature not observed in the data set. The model shows increased ozone in the upper troposphere from stratospheric subsidence at around 150° longitude (equivalent to −210° east longitude) and 190° (equivalent to −170° east longitude). The lidar data show possible ozone intrusions at −180°east and −160°east. These model-measurement comparisons reinforce the point made previously that the PT-A period is much more strongly influenced by episodic events. These events, as described earlier, are tied to biomass burning in the South Africa and South America and possibly to stratospheric subsidence events, as captured by both the model and the lidar data for flight 4 [*Fenn et al.*, 1999].

4.5. Flux Analyses

[35] The mass fluxes of ozone due to advective, convective, and diffusive transport processes were calculated and saved hourly for each of the model grid cells. Additionally, the mass changes in each of the grid cells due to processes in the model, such as chemical production and chemical loss, were also computed and saved as hourly averages. We integrated these fluxes over the Central Pacific area. This Central Pacific region extends from 165°E to 135°W in longitude and from 30°N to 30°S in latitude. We then further divided this region into three "boxes" in the vertical plane, where the lower tropospheric box (LT) was from 0 to 2 km, the midtropospheric box (MT) extended from 2 to 7 km, and the upper tropospheric box (UT) was from 7 to 12 km. The mass fluxes in the three boxes due to different processes are tabulated in Table 3.

[36] Figure 11 shows a schematic layout of a typical box with the arrow indicating the positive direction of the advective fluxes only. Note that the model computes the dry deposition flux as a subgrid-scale diffusional flux which is not included as a downward directed flux in the lowest box, but tabulated separately (Table 3). Figures 12a and 12b are the advective mass fluxes from model calculations averaged for a month over the Central Pacific region for the PT-B and PT-A periods, respectively. All the fluxes shown are the averages for 1 month (20 March to 18 April for PT-B and September for PT-A) of the model simulation. A negative number associated with an arrow indicates fluxes in a direction opposite to that of the arrow. Thus, an arrow associated with a negative flux could be drawn with its tip pointing in the opposite direction. To keep all the flux figures consistent we adopted this plotting scheme for these figures. The advective mass fluxes of ozone in the lower tropospheric box (LT) are directed from east to west during both PT-A and PT-B. In the midtropospheric (MT) and upper tropospheric (UT) boxes, the flux direction changes from east to west are in alignment with the prevailing wind direction of the dominant flow at higher elevations, i.e., the subtropical jet (Figure 1).

[37] From Figures 12a and 12b the following inferences about the change in advective (directional) mass flux from PT-A to PT-B can be made. In the LT box, the east-to-west fluxes decreased by about 23% from PT-A to PT-B, while the north-south fluxes increased by about 92%. The net downward flux into the LT box decreased from PT-A to PT-B by a factor of 3.5. For the MT box, the zonal flux changed from a net gain for the ozone burden in the box to a net loss, as it decreased by about 148% from PT-A to PT-B. The north-south advective flux, on the other hand, increased during PT-B by up to 146% over the PT-A period. The net subsidence of ozone from the MT box to the LT box was only 10% of its PT-A value during the PT-B period. The UT box showed a flux profile similar to that of the MT box, with decreases in the east-west fluxes of about 500% and increase in the north-south fluxes by a factor of 18 for the PT-B period. The net subsidence from UT to MT also decreased by about 25% during PT-B compared with PT-A.

[38] In general, according to Table 3, the period corresponding to PT-B in the model experiences much stronger north-south flux transport of ozone compared with the PT-A period. The second main feature from this budget analysis is the net decrease of ozone burden over the central Pacific region during the PT-B period resulting from a net loss in ozone from the east-to-west fluxes compared with a net increase during the PT-A period from this zonal transport mechanism. The net vertical fluxes for both PT-A and PT-B in the central Pacific are negative, implying subsidence of ozone in this region. However, the strength of this subsidence is much smaller in the model during the PT-B period than during the PT-A period, and the magnitude is smaller by a factor of 3.5 for the LT box in PT-B compared with PT-A. This result is consistent with the conclusion in section 4.4 that PT-A experienced much stronger stratospheric subsidence than PT-B.

[39] The model output was also diagnosed for the impacts of various subgrid-scale processes implemented in the model. The subgrid convective flux during PT-B was entirely a result of deep convection, taking air from the LT box to the UT box (Table 3). The same analysis for the PT-A period showed an even distribution of convective exchange between the LT and MT boxes and between the LT and UT boxes. The net chemical tendency (production minus loss) of odd oxygen ($O_x = O_3 + O(^1D) + O$) was the largest process term in the LT box for both PT-A and PT-B periods. This term yielded a loss of 6584 kg/s during the PT-A period, whereas a loss of 4167 kg/s for the PT-B period, a decrease of 37% for the LT box. The net O_x chemical loss in the MT box remained relatively constant at 1262 kg/s for PT-A to 1554 kg/s for PT-B (an increase of 23% from PT-A

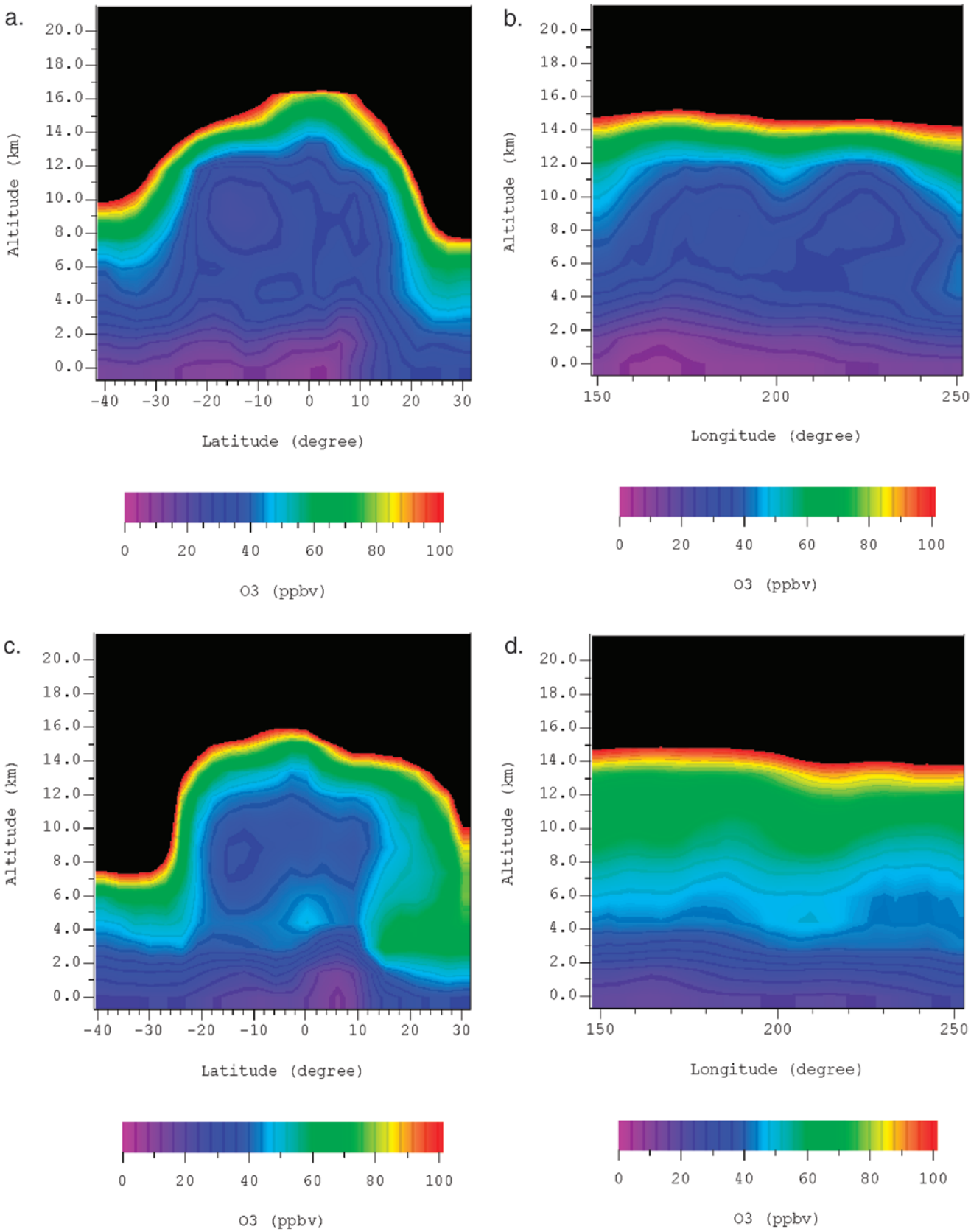
a.
b.
c.
d.
Altitude (km)
20.0
18.0
16.0
14.0
12.0
10.0
8.0
6.0
4.0
2.0
0.0
-40 -30 -20 -10 0 10 20 30
Latitude (degree)
150 200 250
Longitude (degree)
0 20 40 60 80 100
O3 (ppbv)

Table 3. Fluxes of Ozone Over the Central Pacific Region (165°E–135°W, 30°N–30°S) Derived From MOZART (v2)[a]

Monthly Averaged Fluxes, kg/s		Directional Fluxes									
		West	East	South	North	Bottom	Top	Adv	Conv.	Diff.	Chem.
PEM-Tropics A (Sep.)	UT	22,470	20,340	−2,402	−1,896	−1,718	−972	877.6	−1,268	4.329	917.3
	MT	6,486	4,144	−1,456	−2,424	−2,589	−1,718	2,440	−1,443	−2.824	−1,262
	LT	−3,059	−5,060	−28.52	−754.5	0	−2,589	5,316	2,715	−1,287	−6,584
PEM-Tropics B (Mar.)	UT	18,840	27,650	−1,550	−10,510	−654.9	−1,221	710.2	−1,906	6.303	650
	MT	4,551	5,678	−694	−3,484	−571.6	−654.9	1,746	−62.86	−1.879	−1,554
	LT	−2,674	−4,219	−69.02	−1,465	0	−571.6	3,512	1,972	−1,029	−4,167

Net Fluxes		Latitudinal	Longitudinal	Vertical	% change, (B−A)/A × 100%	E-W	N-S	Vert.
PEM-Tropics A (Sep.)	UT	2,130	−506	−746	UT	−514%	1871%	176%
	MT	2,342	968	−871				
	LT	2,001	726	2,589	MT	−148%	188%	110%
PEM-Tropics B (Mar.)	UT	−8,810	8,960	566.1				
	MT	−1,127	2,790	83.3	LT	−22.8%	92%	−78%
	LT	1,545	1,396	571.6				

[a]The directional fluxes refer to the direction toward which the fluxes are directed. Changes in the mass of ozone in a grid box due to subgrid-scale process are listed as: Adv., advective flux; Conv., convective flux; Diff., diffusive flux, including dry deposition for the lower troposphere box; Chem., net change due to chemistry. The altitude range of each of the boxes is designated as UT, upper tropospheric box (7–12 km) as MT, middle tropospheric box (2–7 km), lower tropospheric box (0–2 km) as LT.

to PT-B). The UT box had net chemical production levels of for 917 kg/s (PT-A) and 650 kg/s (PT-B), showing a decrease of 29% from PT-A to PT-B.

[40] The difference in the ozone burden was calculated for each of the boxes at the beginning and end of each month in order to explain the change in mass fluxes shown in Figures 12a and 12b. Ozone burdens in the LT, MT, and UT boxes during the PT-A period were larger than those during the PT-B periods by 35%, 21% and 7%, respectively. The changes in ozone burden calculated by using this procedure for the LT box show increases for the PT-B and PT-A periods by about 0.8 million tons (mt) and 0.5 mt, respectively. The MT ozone burden increased by 0.3 mt during the PT-B period, while it decreased by about 0.2 mt for the PT-A period. The UT ozone burden decreased by about 0.9 mt during the PT-B period and increased by about 2.2 mt during the PT-A period. These figures are broadly consistent with the rest of the flux analyses discussed above.

[41] In summary, the salient features through the flux analysis are (1) increased ozone burden in the region during PT-A compared with PT-B; (2) much stronger transport from the northern hemisphere during the PT-B compared with PT-A; (3) much higher convective transport from the surface to mid and upper troposphere during PT-B compared with PT-A; and (4) most of the ozone in to this central Pacific region came from east-west transport during PT-A compared with north-south pathway during the PT-B period.

[42] Each of these conclusions from the model-derived fluxes supports the general observations regarding the seasonal variations in meteorology, such as the location of the ITCZ and strength of deep convection which were noted in the previous sections.

4.6. Ozone Production and Loss Tendencies

[43] As mentioned earlier, odd oxygen (O_x) production and loss terms were calculated in both the 3-D GCTM as well as in the photochemical box model. The O_x production and loss terms were calculated from the 3-D model every hour as averages for the previous hour from our limited-in-time runs for the March–April and August–September 3-D GCTM runs. In contrast, the box model was calculated with constraints of the measurements during the PT-A and PT-B campaigns. The results of ozone production/loss tendency from the box model and the MOZART 3-D model for the PT-B period are shown in Figures 13a and 13b as a function of altitude and latitude in the tropical region. The 3-D GCTM results represent the daytime average of the production and loss terms averaged over the central Pacific (longitudes from 165°E to 135°W). In general, the 3-D GCTM has the same tendency (i.e., production or loss) as

Figure 10. (opposite) (a) MOZART calculated longitudinally averaged ozone profiles for the PT-B time period. The figure shows results of model calculations, at the nearest spatial location and at local time as the measurements for the months of March and April, subsequently averaged over all longitudes in the respective latitude and altitude bins. (b) MOZART calculated latitudinally averaged ozone profiles for the PT-B time period. The figure shows results of model calculations, at the nearest spatial location and local time as the measurements for the months of March and April, subsequently averaged over all the latitudes in the respective longitude and altitude bins. (c) MOZART calculated longitudinally averaged ozone profiles for the PT-A time period. The figure shows results of model calculations, at the nearest spatial location and local time as the measurements for the months of September, subsequently averaged over all the longitudes in the respective latitude and altitude bins. (d) MOZART calculated latitudinally averaged ozone profiles for the PT-A time period. The figure shows results from the model calculations at the nearest spatial location and local time as the measurements for the months of September, subsequently averaged over all latitudes in the respective longitude and altitude bins.

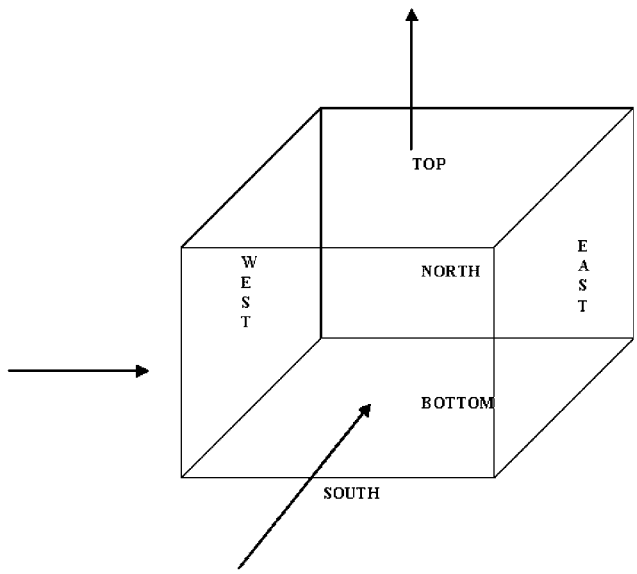

Figure 11. Layout of the box used for making ozone flux and budget analyses with MOZART (v2).

the box model results for most of the altitude and latitude bins. However, the 3-D model produces less ozone in the upper troposphere (8–12 km) than the box model does. This pattern partially results from low NO_x in the 3-D model compared with measurements for the PT-B period at these altitudes. This is also reflected in the higher-than-measured net destruction rates of O_x in the middle and lower troposphere. A detailed comparison of MOZART (version 1) and measured NO_x from various field experiments has been reported by *Emmons et al.* [1997]. The NO_x emissions in MOZART (v2) are not significantly different from the earlier version, and the modeled NO_x is similar to that reported earlier. Improvements in the representation of NO_x emissions in the model are underway for the next version of MOZART. Note that the results for the PT-A period show similar tendencies, and, hence, are not presented here.

4.7. ITCZ and SPCZ

[44] During the intensive PEM-Tropics experiments, pollutants were observed to have a strong latitudinal and longitudinal gradient across the ITCZ and the SPCZ. *Gregory et al.* [1999] analyzed the data from PT-A and tabulated the range of mixing ratios of several trace gases on either side of the ITCZ and SPCZ. In this paper, we only compared the measurements with the 3-D model for the PT-A period, as the ITCZ and the SPCZ were better defined in terms of meteorology or tracer distribution rather than in the PT-B period [*Avery et al.*, 2001; *Fuelberg et al.*, 2001]. The model results were extracted from a simulation for which results were saved every 1-hr for the month of September. The model midnight values were extracted from all longitude grid points in the model from 160°W to 140°W, which corresponds to

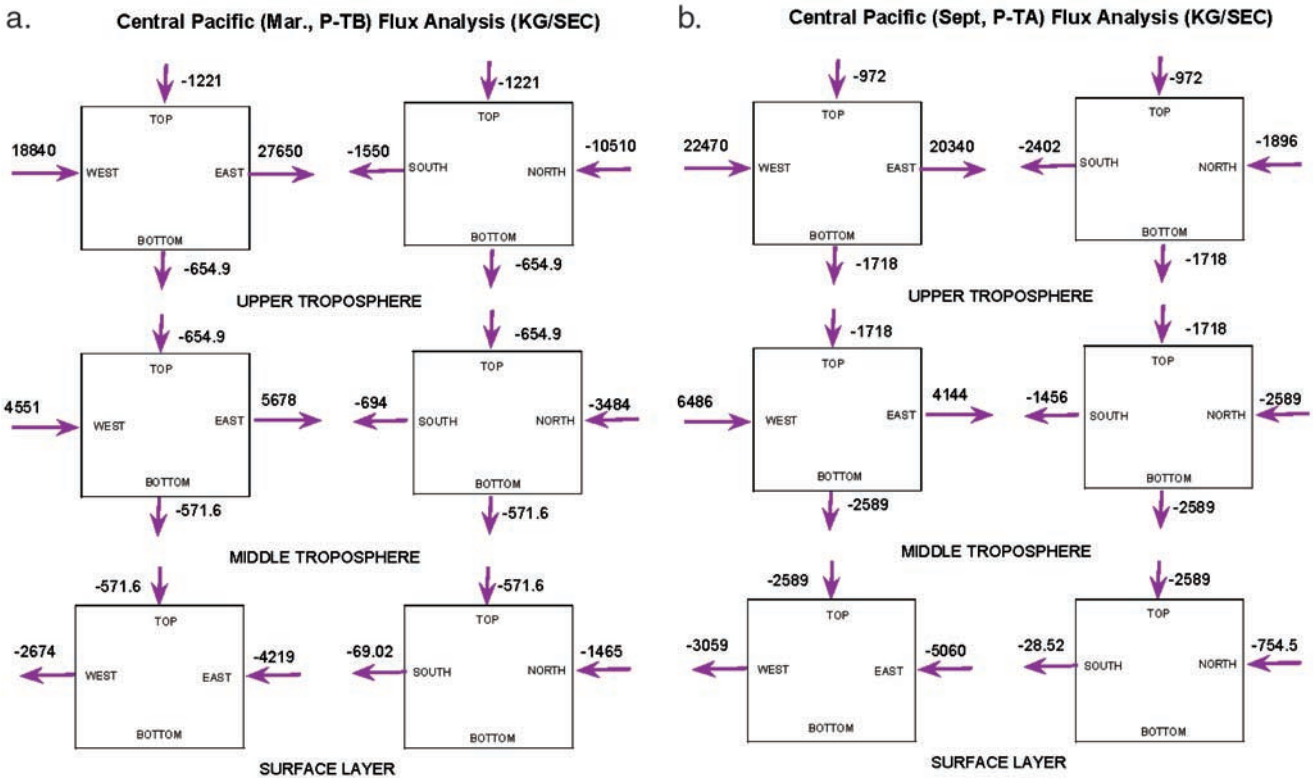

Figure 12. (a) MOZART calculated ozone advective fluxes (kg s^{-1}) for the central Pacific box for the PT-B period (March, April). Arrows show the directions of advective fluxes calculated by the model, and a negative number denotes a flux in a sense opposing the direction of an arrow. (b) MOZART calculated ozone advective fluxes (kg s^{-1}) for the central Pacific box for the PT-A period (September). Arrows show the directions of advective fluxes calculated by the model, and a negative number denotes a flux in sense opposing the direction of an arrow.

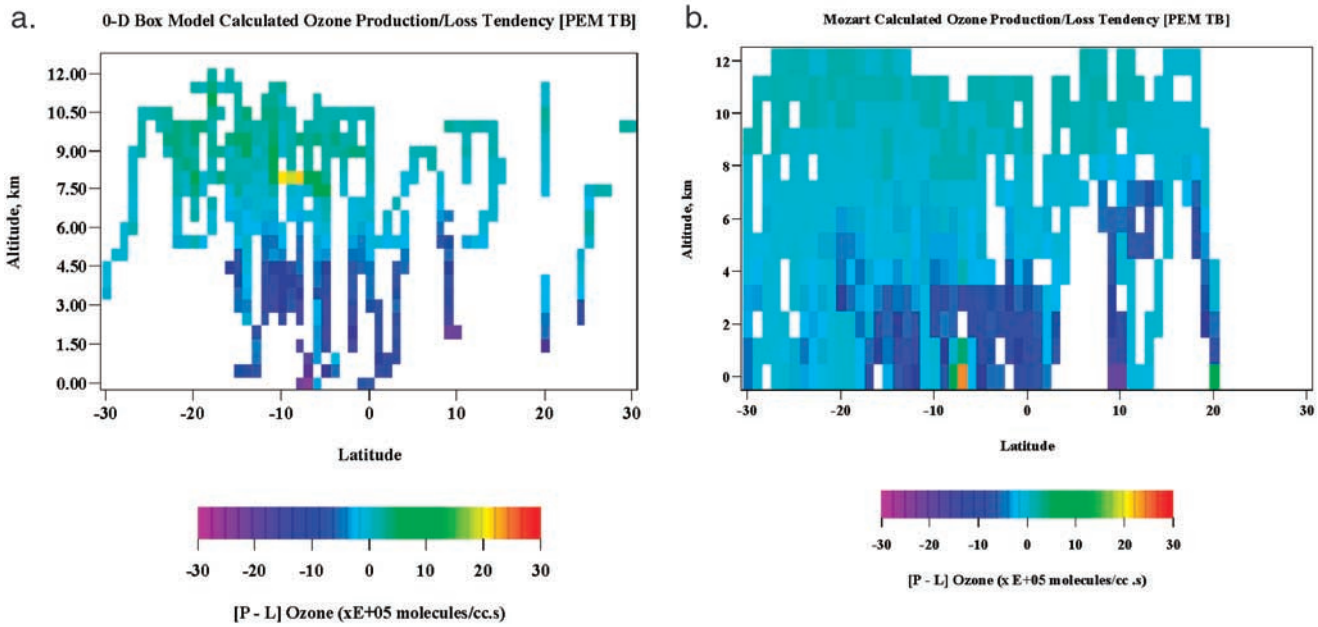

Figure 13. (a) Ozone net production/loss tendency (molecules cm^{-3} s^{-1}) for the 0-D photochemical box model for the PT-B data set. All point measurements were enough constraints for calculating the tendencies exist are shown. If several measurements exist in a given altitude, latitude bin, the average for that bin is plotted. (b) MOZART calculated ozone net production/loss tendency (molecules cm^{-3} s^{-1}) for the PT-B period (March, April). The model results are daytime averages of the tendencies, averaged over the central pacific (longitudes 165°E to 135°E) as a function of latitude.

the approximate local noontime and location of the flight transects across the ITCZ during the PT-A. The model results were then binned in altitude bins ranging from 1 km thick near the surface to 2 km at 10 km. The mixing ratio profiles from 10°N to 10°S latitude in the model were then examined to pick the two profiles with the greatest contrast in the mixing ratios of ozone below 6 km. This procedure yielded 10°N and 1.5°N as the northern side of the ITCZ and the southern side of the ITCZ, respectively, in the model. This is in fair agreement with 14.9°N and 0.5°N for the same locations based on the data by *Gregory et al.* [1999].

[45] Figure 14 shows the model-derived mixing ratios for (1) ozone, (2) CO, (3) C_3H_8/C_2H_6 and (4) C_2H_6/CO for the northern and southern sides of the ITCZ. The figure also shows similarly grouped PT-A measurements from *Gregory et al.* [1999]. It should be noted that all of the measurements shown come from only two flights, flight 4 and flight 19, representing approximately a few hours of observations. The measurements show a distinction in the air mass below 6 km on either side of the ITCZ. The model calculated ozone (Figure 14a) has higher variability than the measurements, as the data were obtained over a wide range of longitudes. The agreement between the measured and modeled ozone is satisfactory below 2 km. The measurements reveal less than 2 ppb of median ozone difference on either side of the ITCZ below 2 km, with the northern side median higher than the southern side. The model calculated differences in the median are of the order 1 ppb, higher in the north than in the south. Above 2 km the southern side has more ozone than the northern side in both the measurements and model results. The delta (south–north) in the measurements is larger than the modeled by 20 to 40%. Thus, there is only a qualitative agreement between the modeled and measured ozone across the ITCZ. The CO in the model below 2 km is marginally higher in the southern side of the ITCZ compared with the northern side and in variance from the measurements (Figure 14b). However, the measured CO is within the range of modeled CO at all the remaining altitude levels.

[46] To further examine the model performance in this region, we calculated the ratios of selected hydrocarbons and compared them with the measurements. The first pair considered for these calculations is the ratio of C_3H_8/C_2H_6, which could be considered as a rough measure of the age of air. Assuming ethane and propane are from similar source regions, a lower ratio signifies older air. Figure 14c shows the ratio calculated by the model and measured on either side of the ITCZ. The measurements indicate fractionally older air (lower ratio) in the south of the ITCZ compared with the north below 1 km. The model calculates older air to the north compared with the south of the ITCZ at this altitude. Between 1 and 8 km the model calculations correspond to measurements. Above 8 km the model calculates much older air than that measured to the north of the ITCZ, whereas the modeled and measured ages to the south of the ITCZ roughly agree.

[47] The second ratio calculated was that of C_2H_6/CO,one that is expected to decrease much more slowly with age than the C_3H_8/C_2H_6 ratio, as the lifetimes of C_2H_6 and CO are of the same order of magnitude. A simple calculation based purely on their chemical loss rates suggests that this ratio would decrease almost half as slowly as the C_3H_8/C_2H_6 ratio. This ratio is lower to the north of the ITCZ relative to the south (Figure 14d), a trend opposite to that calculated by

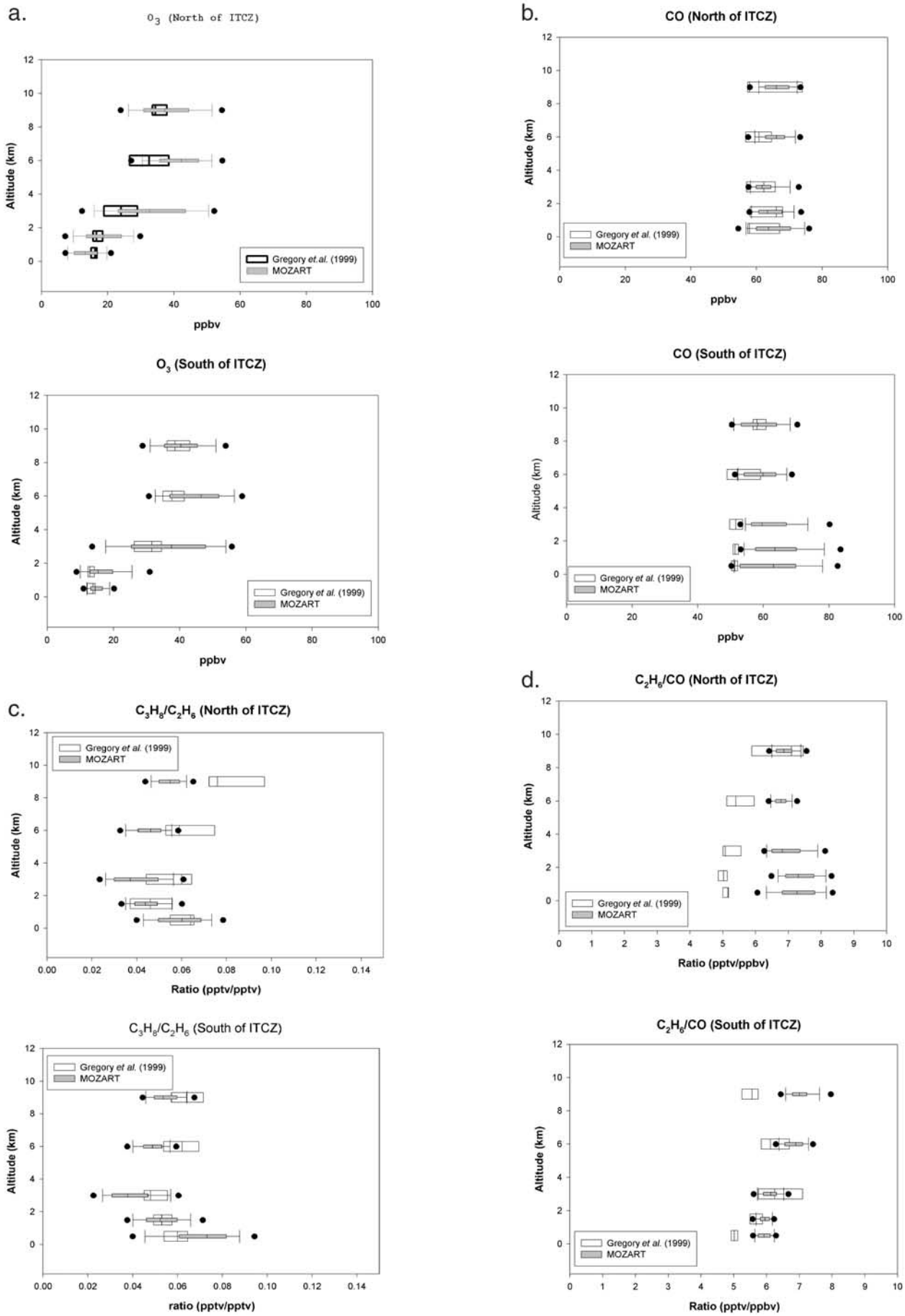
a.
O3 (North of ITCZ)
Altitude (km)
ppbv
Gregory et.al. (1999)
MOZART
b.
CO (North of ITCZ)
Altitude (km)
ppbv
Gregory et al. (1999)
MOZART
O3 (South of ITCZ)
Altitude (km)
ppbv
Gregory et al. (1999)
MOZART
CO (South of ITCZ)
Altitude (km)
ppbv
Gregory et al. (1999)
MOZART
c.
C3H8/C2H6 (North of ITCZ)
Altitude (km)
Ratio (pptv/pptv)
Gregory et al. (1999)
MOZART
d.
C2H6/CO (North of ITCZ)
Altitude (km)
Ratio (pptv/ppbv)
Gregory et al. (1999)
MOZART
C3H8/C2H6 (South of ITCZ)
Altitude (km)
ratio (pptv/pptv)
Gregory et al. (1999)
MOZART
C2H6/CO (South of ITCZ)
Altitude (km)
Ratio (pptv/ppbv)
Gregory et al. (1999)
MOZART

the model. This discrepancy largely results from much higher mixing ratios for ethane in the model to the north of the ITCZ compared with the measurements. The measurements also show unusually low ethane mixing ratios to the north of the ITCZ, more than 100 pptv lower than in the south, below 4 km, whereas the model calculates higher ethane mixing ratios to the north of the ITCZ compared with the south. The model ratio agrees with the measured ratio to the south of the ITCZ up to 8 km, where the modeled ethane approximately agrees with the measurements. However, with this limited set of measurements, it is difficult to state if the observed distribution of ethane is unusual or a recurring feature. As discussed earlier in section 4.1, the model has a weak representation of the SPCZ during both PT-A and PT-B. As a result, we do not expect the model to generate much variation in mixing ratios for the gases as discussed above across the SPCZ, and no further effort was made here to analyze the gradient across this barrier. In summary, the model fairly represents the measured trends of selected trace gases across the ITCZ. The largest discrepancy was calculated for the ratio of C_2H_6/CO, largely resulting from a particularly low mixing ratio of ethane measured on the northern side of the ITCZ compared with the southern side. The model reproduces the key observed feature of a gradient in the lower levels of the atmosphere across the ITCZ in the mixing ratios of ozone, CO and the ratios of key hydrocarbons. The model SPCZ is relatively weak compared with observations, and, as a result, we do not attempt to evaluate this barrier in the current model. The amount of data available to evaluate these two significant feature of tropospheric transport of atmospheric trace gases is insufficient for further evaluation with the current model.

5. Summary and Conclusions

[48] The 3-D GCTM, MOZART, was used to analyze the significant seasonal variations in the concentrations of ozone observed in the southern tropical Pacific during the PT-A (austral spring) and PT-B (austral fall). Diurnal average ozone values from a 1-year model calculation were used for comparison with measured ozone profiles at SHADOZ sites. The model showed fairly accurately reproduced the observed ozone profiles, including the seasonal variability. Another set of model calculations was carried out for the period of August–September and March–April corresponding to the PT-A and PT-B periods, respectively, to produce additional hourly diagnostic outputs, including directional ozone fluxes and in situ production and loss for the O_x group across the model grid surfaces. The O_x production and loss tendencies were also calculated by using a box photochemical model that was constrained with observations. Results were compared with MOZART-calculated values.

[49] The model results for the tropical Southern Hemisphere accurately reproduced the observed low ozone values throughout the depth of the troposphere during the PT-B period. However, the increase in ozone observed in the tropical Northern Hemisphere was shifted further north in the model than in the observations. Further, the pockets of high ozone present in the data set at 10–12 km range were not captured in the model. These features could represent episodes of long-range transport of ozone from source regions, reflecting the transient nature of the emissions or transport. The grid-scale transport derived from climatology seems unlikely to lead to such events. Similarly, the salient feature of the PT-A data set is the frequent occurrence of elevated midtropospheric ozone in the southern tropics. The model showed only a slight elevation in ozone mixing ratios at 25°S to 15°S as compared with the significant elevations in the observations. Sensitivity tests indicate that underrepresentation of biomass burning in the southern tip of Africa or South America could contribute to underprediction of ozone. However, the sensitivity tests were unable to isolate the particular region (i.e., South America or South Africa) that most likely contributed to the observed elevated ozone layers.

[50] In general, the measured ozone and CO during the PT-A period were higher than the measured ones during the PT-B period. The PT-A period, in particular had higher mixing ratios of these gases in the mid-to-upper troposphere in the southern tropics compared with PT-B. The model generally tended to under predicting ozone in this region for both periods. The seasonal behavior in the abundance of these gases in this region, higher values during the PT-A period compared with the PT-B period, was simulated well by the model. Elevated mixing ratios of these gases in certain pockets of air that could be a result of episodic long-range transport were not reproduced, however.

[51] Fluxes of ozone across grid boundaries were computed and analyzed for the PT-A and PT-B periods. In general, the period corresponding to PT-B experienced much stronger north-south flux transport of ozone than did the PT-A period. The budget analysis revealed a net decrease in the ozone burden during the PT-B period, reflecting the net loss in ozone from east-to-west fluxes, compared with a net increase during the PT-A period from this zonal transport mechanism. The grid-scale net vertical fluxes for both the PT-A and PT-B periods in the central

Figure 14. (opposite) (a) Ozone mixing ratios on the northern and southern sides of ITCZ from MOZART (narrow shaded boxes). The PT-A measurements (clear boxes) are as tabulated by *Gregory et al.* [1999]. For MOZART results the central box represents the middle 50% of the data points, while the lines extending from the box represent the upper and lower quartiles. The PT-A measurement box shows the median and the upper and lower quartiles. The shaded circle on either side of the MOZART box represents the outliers, and the median is the thick line inside the box. (b) CO mixing ratios on the northern and southern sides of ITCZ from MOZART (narrow shaded boxes). The PT-A measurements (clear boxes) are as tabulated by *Gregory et al.* [1999]. Descriptions of the boxes are as for (a). (c) Ratio of propane/ethane mixing ratios (pptv/pptv) on the northern and southern sides of ITCZ from MOZART (narrow shaded boxes). The PT-A measurements (clear boxes) are as tabulated by *Gregory et al.* [1999]. Descriptions of the boxes are as for (a). (d) Ratio of ethane/CO mixing ratios (pptv/ppbv) on the northern and southern sides of ITCZ from MOZART (narrow shaded boxes). The PT-A measurements (clear boxes) are as tabulated by *Gregory et al.* [1999]. Descriptions of the boxes are as for (a).

Pacific were negative, implying subsidence of ozone in this region. However, the strength of this subsidence in the model was much smaller during the PT-B period than in the PT-A period and was smaller by a factor of 3.5 for the LT box in PT-B compared with PT-A. The subgrid convective flux during PT-B was entirely a result of deep convection taking air from the LT box to the UT box. The same analysis for the PT-A period verified an even distribution of convective exchange between the LT and the MT boxes and the LT and UT boxes.

[52] Flux analysis demonstrated that there was an increased ozone burden and stronger convective transport from the surface to mid and upper troposphere in the tropical southern Pacific during the biomass-burning season in the Southern Hemisphere (PT-A). In addition, most of the ozone transported in to this region came from zonal transport during PT-A compared with meridional pathway during the PT-B. Over this tropical southern Pacific region, the inter-hemispheric transport during PT-B brings Northern Hemispheric ozone into the Southern Hemisphere much more effectively than during the PT-A time period. The O_x production and loss tendencies from the 3-D model were compared with those from a box photochemical model constrained with the PT-A and PT-B measurements. Overall, the 3-D GCTM obtained the same tendency (i.e., production or loss) as the box model results for most of the altitude and latitude bins. However, the model was much less likely to produce ozone in the upper troposphere (8–12 km) than that could be derived from the data. This pattern partially resulted from low NO_x in the model compared with measurements for the PT-B period in these altitudes. This observation was also reflected in the higher-than-measured net destruction rates of O_x in the middle and lower troposphere.

[53] Finally, the model qualitatively represents variations of selected trace gases across the ITCZ, although quantitative features of this variability are reproduced much less successfully. The largest discrepancy was calculated for the ratio of C_2H_6/CO, largely resulting from a particularly low mixing ratio of ethane measured on the northern side of the ITCZ compared with its southern side. The model SPCZ is relatively weak compared to that was observed, and as a result we do not attempt to evaluate this barrier in the current model.

[54] In conclusion, the model was able to capture the main aspects of the seasonal variability of ozone in this region, which was shown to be a result of much larger transport of ozone into this region from east-west zonal transport during the austral spring compared to fall. The inter-hemispheric transport from the north to the south was smaller during the austral spring compared to fall and hence not the cause of the increase in ozone burden in this region during the austral spring compared to the fall season. Model sensitivity tests reveal that the biomass-burning emissions in the model may be underestimated. Future versions of the model will address these issues in detail.

[55] **Acknowledgments.** This work was supported by National Aeronautical and Space Administration (NASA) under a grant to the University of Illinois through the PEM project (NCC-1-309) and by the EPA STAR program (CX825749-01). The work at Argonne National Laboratory was supported by NASA under interagency agreement, through U.S. Department of Energy contract W-31-109-ENG-38. Initial testing and acquisition of the 3-D MOZART model is supported by a grant from EPA (R826384-01). We would also like to thank the National Center for Supercomputing Applications (NCSA) at the University of Illinois, Urbana-Champaign, for providing the computing time and Dr. Guy Brasseur and staff of the Atmospheric Chemistry Division at NCAR for collaboration with MOZART. We would also like to thank the editor and reviewers for their useful comments, which greatly helped to clarify the manuscript.

References

Avery, M. A., D. J. Westberg, H. E. Fuelberg, R. E. Newell, B. E. Anderson, S. A. Vay, G. W. Sachse, and D. R. Blake, Chemical transport Across the ITCZ in the Central Pacific during and ENSO cold phase event in March/April of 1999, *J. Geophys. Res.*, *106*(D23), 32,539–32,553, 2001.

Blake, N. J., et al., Influences of southern hemispheric biomass burning on mid-tropospheric distributions of nonmethane hydrocarbons and selected halocarbons over the remote South Pacific, *J. Geophys. Res.*, *104*, 16,213–16,232, 1999.

Brasseur, G. P., D. A. Hauglustaine, S. Walters, P. J. Rasch, J. F. Muller, C. Ganier, and X. X. Tie, MOZART: A global chemical transport model for ozone and related chemical tracers, part 1, Model description, *J. Geophys. Res.*, *103*, 28,265–28,289, 1998.

Browell, E. V., et al., Large-scale air mass characteristics observed over the remote tropical Pacific ocean during March–April 1999: Results from PEM Tropics B field experiment, *J. Geophys. Res.*, *106*(D23), 32,481–32,501, 2001.

Crawford, J., et al., Photostationary state analysis of the NO_2-NO system based on airborne observations from the western and central North Pacific, *J. Geophys. Res.*, *101*, 2053–2072, 1996.

Davis, D. D., et al., Assessment of ozone photochemistry in the western North Pacific as inferred from the PEM-West A observations during the fall 1991, *J. Geophys. Res.*, *101*, 2111–2134, 1996.

DeMore, W. B., S. P. Sander, D. M. Golden, R. F. Hampson, M. J. Kurylo, C. J. Howard, A. R. Ravishankara, C. E. Kolb, and M. J. Molina, Chemical kinetics and photochemical data for use in stratospheric modeling, Evaluation 12, *Publ. 97-4*, Natl. Aeronaut. and Space Admin., Jet Propul. Lab., Pasadena, Calif, 1997.

Emmons, L. K., et al., Climatologies of NO_x and NO_y: A comparison of data and models, *Atmos. Environ.*, *31*, 1851–1904, 1997.

Fenn, M. A., E. V. Browell, G. L. Gregory, B. G. Heikes, M. G. Schultz, D. R. Blake, J. E. Dibb, S. T. Sandholm, and R. W. Talbot, Chemical characteristics of air from differing source regions during the Pacific Exploratory Mission-Tropics A (PEM-TROPICS A), *J. Geophys. Res.*, *104*, 16,197–16,212, 1999.

Fuelberg, H. E., R. E. Newell, S. P. Longmore, Y. Zhu, D. J. Westberg, E. V. Browell, D. R. Blake, G. L. Gregory, and G. W. Sachse, A meteorological overview of the Pacific Exploratory Mission (PEM) Tropics period, *J. Geophys. Res.*, *104*, 5585–5622, 1999.

Fuelberg, H. E., R. E. Newell, D. J. Westberg, J. C. Maloney, J. R. Hannan, B. C. Martin, M. A. Avery, and Y. Zhu, A meteorological overview of the second Pacific Exploratory Mission in the Tropics, *J. Geophys. Res.*, *107*(D23), 32,427–32,443, 2001.

Giorgi, F., and W. L. Chameides, The rainout parameterization in a photochemical model, *J. Geophys. Res.*, *90*, 7872–7880, 1985.

Grant, K. E., K. E. Taylor, J. S. Ellis, D. J. Wuebbles, Status of the infrared radiation submodels in the LLNL 1-D and 2-D chemical-transport models, *UCID-21146*, Lawrence Livermore Natl. Lab., Livermore, Calif., 1987.

Gregory, G. L., et al., Chemical characteristics of Pacific tropospheric air in the region of the intertropical convergence zone and the South Pacific convergence zone, *J. Geophys. Res.*, *104*, 5677–5696, 1999.

Hack, J. J., Parameterization of moist convection in the National Center of Atmospheric Research Community Model (CCM2), *J. Geophys. Res.*, *99*, 5551–5568, 1994.

Hauglustaine, D. A., G. P. Brasseur, S. Walters, P. J. Rasch, J.-F. Muller, L. K. Emmons, and M. A. Carroll, MOZART: A global chemical transport model for ozone and related chemical tracers, part 2, Models results and evaluations, *J. Geophys. Res.*, *103*, 28,291–28,335, 1998.

Hindmarsh, A. C., ODEPACK, A systemized collection of ODE solvers, *Scientific Computing*, edited by R. S. Stepleman et al., North-Holland, Amsterdam, 1983.

Hoell, J. M., D. D. Davis, S. C. Liu, R. Newell, M. Shipman, H. Akimoto, R. J. McNeal, R. J. Bendura, and J. W. Dewry, Pacific Exploratory Mission-West A (PEM-West A): September–October 1991, *J. Geophys. Res.*, *101*, 1641–1653, 1996.

Hoell, J. M., D. D. Davis, S. C. Liu, R. Newell, M. Shipman, H. Akimoto, R. J. McNeal, R. J. Bendura, and J. W. Dewry, Pacific Exploratory Mission- West B (PEM-West B): February–March 1994, *J. Geophys. Res.*, *102*, 28,223–28,239, 1997.

Hoell, J. M., D. D. Davis, D. J. Jacob, M. O. Rodgers, R. E. Newell, H. E. Fuelberg, R. J. McNeal, J. L. Raper, and R. J. Bendura, Pacific Explora-

tory Mission in the tropical Pacific (PEM-Tropics A): August–September 1996, *J. Geophys. Res.*, *104*, 5567–5583, 1999.

Holtslag, A., and B. Bonville, Local versus nonlocal boundary-layer diffusion in a global climate model, *J. Clim.*, *6*, 1825–1842, 1993.

Hurrell, J. W., J. J. Hack, B. A. Boville, D. L. Williamson, and J. T. Kiehl, The dynamical simulation of the NCAR community climate model version 3 (CCM3), *J. Clim.*, *11*, 1207–1236, 1998.

Jacob, D. J., et al., Origin of ozone and NO_x in the tropical troposphere: A photochemical analysis of aircraft observations over the South Atlantic basin, *J. Geophys. Res.*, *101*, 24,235–24,250, 1996.

Jacobson, M. Z., and R. P. Turco, SMVGEAR: A sparse-matrix vectorized GEAR code for atmospheric models, *Atmos. Environ., Part A*, *28*, 273–284, 1994.

Kotamarthi, V. R., et al., Evidence of heterogeneous chemistry on sulfate aerosols in stratospheric air masses measured in PEM-West B, *J. Geophys. Res.*, *102*, 28,425–28,436, 1997.

Kotamarthi, V. R., D. J. Wuebbles, and R. A. Reck, Effects of non-methane hydrocarbons on lower stratospheric and upper tropospheric 2-D zonal average model climatology, *J. Geophys. Res.*, *104*, 21,537–21,547, 1999.

Lin, S.-J., and R. B. Rood, Multidimensional flux-form semi-Lagrangian transport schemes, *Mon. Weather Rev.*, *134*, 2046–2070, 1996.

Maloney, J. C., H. E. Fuelberg, M. A. Avery, B. G. Heikes, D. R. Blake, J. E. Dibb, S. T. Sandholm, and R. W. Talbot, Chemical characteristics of air from different source regions during the second Pacific Exploratory Mission to the Tropics (PEM Tropics B), *J. Geophys. Res.*, *106*(D23), 32,609–32,625, 2001.

Muller, J.-F., and G. Brassuer, IMAGES: A three-dimensional chemical transport model for the global atmosphere, *J. Geophys. Res.*, *100*, 16,445–16,490, 1995.

NARSTO *Research Strategy and Organization Management Plan*, external review draft, U.S. Environ. Prot. Agency, Research Triangle Park, N. C., 1994.

Olivier, J. G. J., A. F. Bouwman, C. W. M. van der Maas, J. J. M. Berdowski, C. Veldt, J. P. J. Bloos, A. J. H. Visschedijk, P. Y. J. Zandveld, and J. L. Haverlag, Description of EDGAR version 2.0: A set of global emission inventories of greenhouse gases and ozone-depleting substances for all anthropogenic and most natural sources on a per country basis and on a 1 × 1 degree grid, *RIVM Rep. 771060 002/TNO-MEP Rep. R96/119*, Natl. Inst. of Public Health and the Environ., Bilthoven, Netherlands, 1996.

Olson, J. R., B. A. Baum, D. R. Cahoon, and J. H. Crawford, Frequency and distribution of forest, savanna, and crop fires over tropical regions during PEM-Tropics A, *J. Geophys. Res.*, *104*, 5865–5875, 1999.

Patten, K. O., Z. Li, and D. J. Wuebbles, Estimates of atmospheric lifetimes and ozone depletion potentials for the bromopentafluoropropane isomers, *J. Geophys. Res.*, *105*, 11,625–11,631, 2000.

Raper, J. L., M. M. Kleb, D. J. Jacob, D. D. Davis, R. E. Newell, H. E. Fuelberg, R. J. Bendura, J. H. Hoell, and R. J. McNeal, Pacific Exploratory Mission in the Tropical Pacific: PEM-Tropics B, March–April 1999, *J. Geophys. Res.*, *106*(D23), 32,401–32,425, 2001.

Schultz, G. M., et al., On the origin of troposphere ozone and NO_x over the tropical South Pacific, *J. Geophys. Res.*, *104*, 5829–5844, 1999.

Staudt, A. C., D. J. Jacob, J. A. Logan, D. Bachiochi, T. N. Krishnamurti, and N. I. Poisson, Global chemical model analysis of biomass burning and lightning influences over the South Pacific in austral spring, *J. Geophys. Res.*, *107*(D14), 4200, doi:10.1029/2000JD000296, 2002.

Thompson, A. M., and J. C. Witte, SHADOZ (Southern Hemisphere ADditional Ozonesondes): A new data set for the earth science community, *Earth Obs.*, *11*(4), 27–30, 1999.

Williamson, D. L., and P. J. Rasch, Two dimensional, semi-Lagrangian transport with shape preserving interpolation, *Mon. Weather Rev.*, *117*, 102–129, 1989.

World Meteorological Organization (WMO), *Scientific Assessment of Ozone Depletion: 1994*, *Rep. No. 37*, Global Ozone Res. and Monit. Proj., U. N. Environ. Program, Geneva, 1995.

Zhang, G. J., and N. A. McFarlane, Sensitivity of climate simulations to the parameterization of cumulus convection in the Canadian Climate Center general circulation model, *Atmos. Ocean*, *33*, 407–446, 1995.

M. A. Avery, E. V. Browell, and G. W. Sachse, NASA-Langley Research Center, Hampton, VA, USA.

D. R. Blake, University of California, Irvine, CA, USA.

L. W. Horowitz, GFDL, Princeton, NJ, USA.

V. R. Kotamarthi, Argonne National Laboratory, Argonne, IL, USA. (vrkotamarthi@anl.gov)

O. J. Ogunsola, C.-F. Wei, and D. J. Wuebbles, Department of Atmospheric Sciences, University of Illinois, Urbana-Champaign, IL, USA.

S. Walters, NCAR, Boulder, CO, USA.